Semi-automatic mapping of shallow landslides using free Sentinel-2 and Google Earth Engine.

Davide Notti. [1], Martina Cignetti. [1], Danilo Godone. [1], Daniele Giordan. [1]

5   [1] Institute for Geo-Hydrological Protection (IRPI), Italian National Research Council (CNR), Torino, Strada Delle Cacce 73, 10135, Italy

Correspondence to: Danilo Godone (danilo.godone@irpi.cnr.it)

Abstract. The global availability of Sentinel-2 data and the widespread coverage of free-cost and high-resolution images nowadays give opportunities to map, at low-cost, shallow landslides triggered by extreme events (e.g. rainfall,

10   earthquake). A rapid and low-cost shallow landslides mapping could improve damages estimations, susceptibility models or land management.

This work presents a semi-automatic methodology to map potential landslides (PL) using Sentinel-2 images, and it is the first step toward more detailed mapping. We create a GIS-based and user-friendly methodology to extract PL based on pre- post- event NDVI variation and geomorphological filtering. The semi-automatic inventory was compared with

15   benchmark landslides inventory drawn on high-resolution images. We also used the Google Earth Engine scripts to extract the NDVI time series and make a multi-temporal analysis.

We apply this to two study areas in NW Italy hatted in 2016 and 2019 by extreme rainfall events. The results show that the semi-automatic mapping based on Sentinel-2 allows detecting the majority of shallow landslides larger than satellite ground pixel (100 m^2). PL density and distribution well match with the benchmark. However, the false positives (30% to

20   50% of cases) are challenging to filter, especially when they correspond to river bank erosions or cultivated land.

Keywords: NDVI, Google Earth Engine, rapid mapping, Sentinel-2, Shallow landslides.

1. Introduction

One of the recent and forecasted impacts of climate change is the rise of extreme meteorological events (IPCC, 2014).

25   During flash floods, one of the most common phenomena is the activation of shallow landslides (Gariano and Guzzetti, 2016). Unfortunately, shallow landslides are not triggered only by rainfall but also by other extreme events like earthquakes (Sassa et al., 1996) or rapid snow melting (Cardinali et al., 2000). These slope instabilities usually involve soils and superficial deposits and represent a meaningful impact on infrastructures and cultivated areas. The pervasive distribution of these phenomena on slopes, hereafter mentioned as extreme events, makes their identification and mapping

30   crucial for effective damage evaluation. For this reason, the definition of procedures and strategies aimed to map shallow landslides has been deeply investigated in the last decades to reach different final goals like: i) the mapping of the full extent of a landslide disaster (Guzzetti et al., 2004); ii) geomorphological and erosion studies (Fiorucci et al., 2011); iii) the validation of susceptibility models (Bordoni et al., 2015; Cignetti et al., 2019; Rossi et al., 2010); iv) the statistical comparison of landslides inventories from different methodologies and sensors (Carrara, 1993; Fiorucci et al., 2018).

35   Landslide event-inventory maps are commonly implemented using several different methodologies: i) post-event aerial photos analysis and plotting (Cardinali et al., 2000); ii) manual or automatic identification based on the use of high-

resolution digital elevation models (DEMs) obtained from airborne LiDAR surveys done after the event (D'Amato Avanzi et al., 2015) (Giordan et al., 2017); iii) traditional geomorphological field surveys (Pepe et al., 2019). In the last years, even satellite images have been used to identify and map shallow landslides (Ghorbanzadeh et al., 2021; Lu et al.,

40   2019; Martha et al., 2010; Mondini et al., 2011; Qin et al., 2018). This recent evolution has been possible thanks to the robust improvement of satellite resolution that nowadays are not so different compared to aerial images (Fiorucci et al., 2019). Recent studies are mostly based on commercial high-resolution satellite images. The use of these commercial images often requires a dedicated acquisition planning after the event that needs a high cost and limits the use of these systems. For instance, areas with low human or infrastructure presence are often overlooked by authorities that mainly

45   dedicate funds to study more inhabited sectors. The scarcity of resources creates a bias between high-income populated areas and remote areas or developing countries that cannot afford the cost.

In the last years, the Sentinel satellites constellation of the Copernicus program made available medium-high resolution images (about 10 m) both multi-spectral (Sentinel-2) and SAR (Sentinel-1) free of cost, and with a high-frequency revisit. In addition, several areas of the world are covered by multi-temporal very-high-resolution images of GoogleEarth™ that

50   could help to detect and map shallow landslides when pre- and post- event images are available (Borrelli et al., 2015). Google Earth Engine (GEE) cloud processing (Gorelick et al., 2017) could also be used to create time series of several satellite data(Optical, SAR), which are useful to detect the change and the recovery of vegetation and to map landslides and their effect on vegetated areas (Scheip and Wegmann, 2021; Yu et al., 2018; Handwerger et al., 2022).

In this work, leveraging on the pre- and post-event NDVI based on Sentinel-2 data, we implemented a dedicated

55   methodology to detect potential shallow landslides semi-automatically. The presented methodology aims to be a user-friendly tool, based on free data and open source software (Notti et al., 2018), easy to replicate for other regions affected by shallow landslides. We subsequently compared potential landslides with a benchmark inventory, manually mapped on post-event high-resolution images. By exploiting GEE, we also create NDVI time series aimed at identifying the most suitable images for detecting potential landslides and monitoring vegetation recovery in the affected areas. Finally, the

60   comparison with other ancillary data allowed us to make some statistics about landslides distributions and density and the triggering factors.

The implemented methodology has been tested in two areas of north-western Italy hit by extreme rainfall events in recent years, *i.e.,* November 2016 and October 2019. The two events triggered hundreds of shallow landslides in small areas, causing widespread damage to the road network, cultivation and, in some cases, urban areas.

65   Semi-automatic and manual inventories and GEE scripts are also published online and open for improvement by the scientific and user community.

2. Study areas

The two presented case studies are located in NW Italy, and were respectively affected by two heavy rainfall events in November 2016 and October 2019.

70   The 2016 event area (about 350 km^2) is located in the Ligurian Alps at the border between Liguria and Piemonte regions (NW Italy). The shape and the extension of the study area (Figure 1) are a combination of: i) the area most hit by rainfall, ii) other literature studies of the event (Cremonini and Tiranti, 2018; Pepe et al., 2019), iii) the footprint of the available Sentinel-2 cloud-free images and the post-event Google Earth image. The area of interest (AOI), henceforth called Tanarello and Arroscia valleys, shows an elevation up to 2500 m a.s.l., and a wide range of land use and vegetation cover

75   from the Mediterranean to the alpine environment. The area intersects several river basins, and the main catchments are

the Tanaro-Tanerello, part of the Po river Basin and the Arroscia stream flowing to the Ligurian Sea. From the geological point of view (Figure 1 B), the northern sector of the area is occupied by the Briançonnaise Zone of the middle Pennidic nappe. This unit is represented by limestone-dolomite, which creates steep slope, conglomerate and volcanic formation (rhyolite). In the southern part of the area, outcrop the Helminotod flysch formations of Monte Saccarello-San Remo,

80 made by limestone-clay sequence, and the sandstone-siltstone sequence of San Bartolomeo formation (Lanteaume et al., 1990; Pepe et al., 2015). The Tanarello and Arroscia valleys area has a sparse human settlement and low population density, ranging from 40 to 1 inhabitant per square kilometres. Most of the inhabitants live in the town of Ormea and Pieve di Teco. Most of the area is occupied by broadleaf forests in the lower part and coniferous forest, grassland and pasture at high altitudes.

85 The area affected by the heavy rainfall event in 2019 (about 530 km^2) is located between the Bormida river and Lemme valleys, in the Southern-east Piemonte region. The considered area has been delimited considering the effects of the event based on the rainfall data, image coverage and reports on damages. The study area mostly overlaps with the Tertiary Piedmont Basin (TPB): a sedimentary succession from Oligocene conglomerates in the South to Pliocene mudstone in the Northern part (Figure 2 B). Three main geological formations outcrop in the detailed training areas, from South to

90 North: the Cortemillia formation (made by Arenite, Mudstone); the Cessole Marls (made by carbonate-rich mudstone, arenite); the Serravalle Formation (made by arenite and sandstone). The southern part is occupied by ophiolitic rocks of the Ligurian oceanic unit (Piana et al., 2017). Alluvial quaternary deposits occupy the bottom of the valley. Several small creeks cross the study area with S-N directions that, in the 2019 event, caused flash floods (Mandarino et al., 2021). The geomorphology of the area is characterized by the presence of a hilly landscape with a more steep slope in the Serravalle

95 Formation, in the northern sector. The vineyards (region of Gavi grape) are mainly located in the central and southern part of the study area (Cessole Marl formations). In contrast, the northern-western part is mainly covered by broadleaf forest, sclerophyllous vegetation and shrubs. Several villages and the small town of Gavi are located inside the AOI, henceforth called Gavi area. The Castle of Gavi hill was particularly hit by shallow landslides, as also occurred in 2014, 1977 and 1935 events (Govi, 1978; Mandarino et al., 2021).

100

2.1 The 20-25 November 2016 event in Tanarrello and Arroscia valleys.

Historical information tells us that the Liguria region and NW Alps have been affected by several extreme rainfall events, usually during autumn (D'Amato Avanzi et al., 2015; Cevasco et al., 2014; Ferrari et al., 2021; Roccati et al., 2018; Guzzetti et al., 2004; Luino, 1999). Recently, global warming and the related sea temperature increase caused a likely

105 positive trend of extreme rainfall events in the area of the Ligurian sea, especially on a short time interval (Gallus Jr et al., 2018; Paliaga and Parodi, 2022; Roccati et al., 2020). From 20 to 25 November 2016, a low-pressure area affected the western Mediterranean Sea (Nimbus Web Eventi Meteorologici, 2022), causing heavy and persistent rainfall that hit NW Italy, and with high severity, the Ligurian Alps. The upper valleys of Tanarello and Arroscia streams (at the border between Liguria and Piemonte regions) were the most hit by this event, and the rainfall accumulation reached 650 – 700

110 mm (Figure 1 C). The rain gauge station of Piaggia peak up to a value of 690 mm, which is far higher than previous flood events of the last 70 years (Figure 1 D). The dense network of rainfall gauges of ARPA Piemonte and ARPA Liguria (the regional agencies for environmental protection) allowed to create an almost accurate map of accumulated rainfall and compare time series of precipitation for some stations. This heavy rainfall triggered many shallow landslides partly mapped with field surveys in Arroscia valley (Pepe et al., 2019). Also, deeper landslides were triggered, like in the case

115 of the villages Monesi di Mendatica, which were partly destroyed by such kind of landslide (ARPA Piemonte, 2018; Notti

Natural Hazards
and Earth System
Sciences

Discussions

et al., 2021). Despite the limited human presence, the damages are estimated in several Millions of Euros only for public infrastructures.
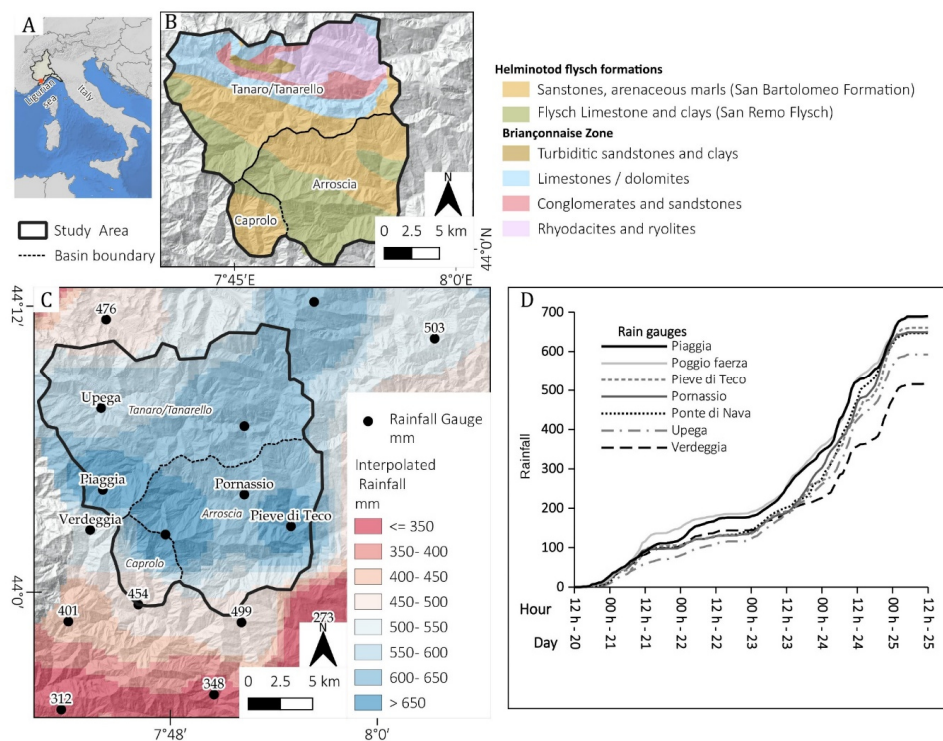
Figure 1. Arroscia/Tanarello November 2016 event. A) Location of the study area; B) Simplified geological map based on (Lanteaume et al., 1990) C) Accumulated rainfall from 20 to 25 November 2016 in the study area. D) Hourly cumulated rainfall for some rain gauge stations of study areas. (Rainfall source: ARPA Piemonte and ARPAL Liguria), Hillshade of map B and C are based DTM of ARPA Piemonte and Regione Liguria.

2.2 the 21-22 October 2019 event in Gavi area.

The October to December 2019 period has been characterized by numerous meteorological events that hit NW Italy, causing an extreme rainy period (Copernicus Climate Change Service, 2019). In particular, on 19-21 October 2019, an extreme rainfall event hit an area between Liguria and Piemonte region, causing severe floods and diffuse shallow landslides in the basins of the Orba and Bormida rivers (Mandarino et al., 2021). This event was caused by a semi-stationary V-shape storm over a relatively small area with extreme rainfall (Figure 2 C) both in intensity and quantity (Mercalli, 2019). This event activated many shallow and deep landslides. In particular, we focused on the area near the town of Gavi where the rain gauge registered about 480 mm/24h, and most of the rainfall (318 mm) was concentrated in six hours intervals (Figure 2 D) (Meteologix, 2022). It is one of the highest rainfall records in the Piemonte region, just five years after that, a previous extreme rainfall hit the same area. The extreme rainfall events of autumn 2019 caused estimated damages of 16 M of Euros in the province of Alessandria (Regione Piemonte - flood events 2019, 2021). After the October 2019 event, a particularly wet period until December 2019 triggered other shallow landslides in the study area.
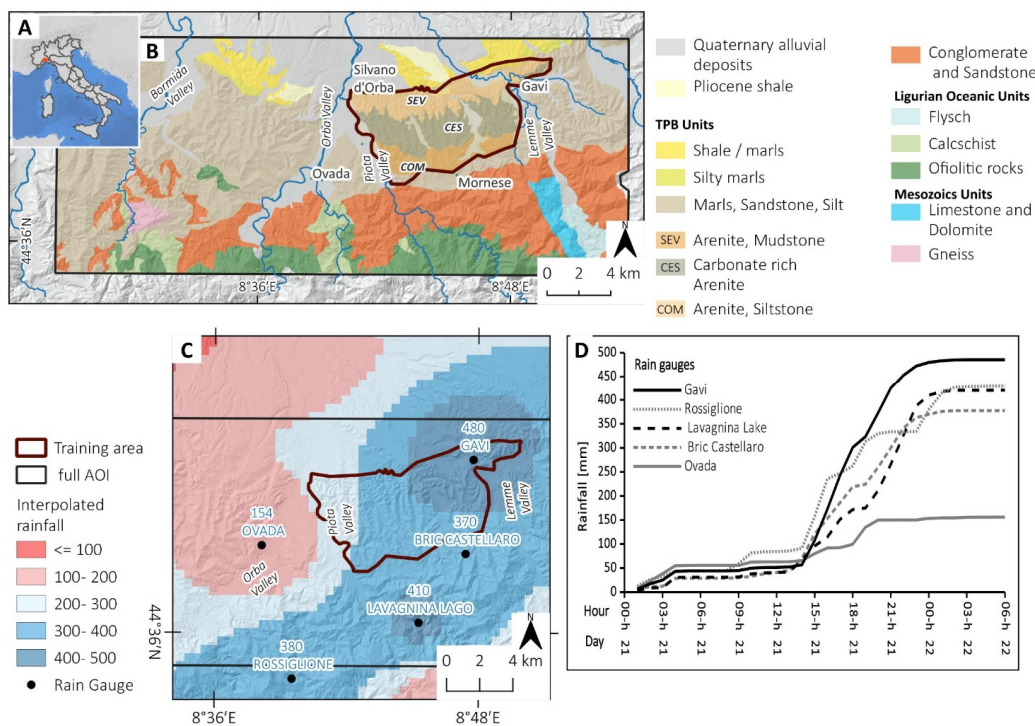
Figure 2. Gavi October 2019 Event. A) Location of the study area; B) Simplified lithological map of the study area based on (Piana et al., 2017); C) Accumulated rainfall from 21 to 22 October 2019 event. D) Hourly cumulated rainfall for some rain gauge stations of study areas. (Rainfall eata source: ARPA Piemonte), Hillshade of map B and C are based DTM of ARPA Piemonte.

3. Materials and Methods.

One of the main effects caused by the activation of shallow landslides is the reduction of vegetation cover that creates a radiometric signature variation often detected by multispectral satellites. Thus, the NDVI is one of the most used band indexes to detect these variations (Fiorucci et al., 2019; Lu et al., 2019; Mondini et al., 2011). For this reason, we create a semi-automatic methodology that deals with pre- and post-event NDVI variation based on free satellite images with the best spatial resolution (Sentinel-2, nowadays).

Our methodology, resumed in Figure 3, aims to produce an inventory of potential shallow landslides (PL) based on NDVI and geomorphological filters. The proposed method identifies areas most affected by shallow landslides that can furtherly be used to support the identification and map of landslides on very-high-resolution images. Time series of NDVI computed on GEE were also used to evaluate the vegetation recovery.

3.1 Potential landslides detection methodology

The proposed methodology (Figure 3) is aimed to create a PL inventory based on the semi-automatic procedure. The mapping method is based on the availability of pre- and post-event satellite images. This methodology is intended to detect surface changes, which are signs of potential shallow landslides, between pre- and post-event images. The PL inventory is aimed to delimit the area most affected by shallow landslides and support a subsequent, detailed landslide

mapping on high-resolution images. The PL is not a geomorphological landslide inventory because the shape of PL is extracted with a semi-automatic procedure and based on middle-resolution images. The PL inventory is created in three main steps: i) satellite images selection; ii) calculation of the Normalised Difference Vegetation Index variation

160 (NDVI$_{var}$), and definition of empirical NDVI$_{var}$ threshold that is adopted for the potential landslide mapping; iii) implementation of a filter using slope and other geomorphological parameters to obtain the potential landslide (PL) inventory and the PL density maps. Thus, the PL inventory is compared over a training area covered by high-resolution images, with a manually drawn dataset, i.e., manual landslides (ML). This comparison phase is important because is used for checking the efficiency of PL methodology and refining the calibration of adopted parameters with iteration processes

165 to improve the quality of the final PL inventory, reducing errors. The proposed methodology is exclusively based on free-cost software (*e.g.* QGIS (QGIS Association., 2022), SAGA GIS (Conrad et al., 2015), R(R Core Team, 2020)) and cloud computing (*e.g.* GEE). In the following sections, the procedure is discussed in more detail.

3.1.1 Satellite Image selection.

170 The first step is the selection of the best pairs of pre- and post-event satellite images aimed to make a change detection analysis. Nowadays, the free satellite images with the best resolution are Sentinel-2 (10 m visible and near-infrared bands) followed by Landsat ones (30 m).

We search for images and filter images using the following criteria:

    i.   cloud cover < 5%;

175   ii.   images acquired in the same period of the year to minimise the effect of shadow and canopy cover change related to season;

    iii.   only summer images (from June to September, in N Emisphere) to have strong contrast in NDVI, no snow coverage, and short shadow.

180 To improve the search for the best pair of images, we also used output from a GEE processing based on the code developed by (Nowak et al., 2021). The processing calculates an averaged NDVI time series from a satellite images collection (e.g. Sentinel-2) filtered by cloud cover, over selected sample polygons that can be directly drawn on the satellite map interface of GEE. The time series plotted in a GEE chart can be exported to a CSV file for further filtering (e.g. replicate date removal) and analysis. We obtained a limited number of pairs of pre- and post- event images with these constraints.

185

3.1.2 NDVI$_{var}$ calculation and threshold

In the second step, we calculated NDVI$_{var}$ by computing the NDVI variation between the pre- and post-event conditions (equation 1). The aim is to identify areas with decreased NDVI values due to vegetation removal or damage caused by

190 shallow landslides. Using the raster calculator of QGIS software, we computed the NDVI using the NIR and the red band.

$$\text{NDVI}_{\text{VAR}} = \text{NDVI}_{\text{post}} - \text{NDVI}_{\text{pre}} \text{ Where NDVI} = (\text{NIR} - \text{Red})/(\text{NIR} + \text{Red}) \tag{1}$$

Then we manually select NDVI$_{var}$ threshold that best identifies changes related to landslides. This threshold does not have

195 a fixed value. It is determined by an operator based on the visual pattern of NDVI$_{var}$, the evidence on the NDVI times series of GEE, and the calibration of the parameters based on PL/ML inventories comparison.

3.1.3 Geomorphological filtering to create PL inventory.

200   In the third step, the results coming from $NDVI_{var}$ are filtered using geomorphological parameters (Table 2). We first used the slope derived from DTM (download from Regione Piemonte and Liguria databases) to filter out the areas with a slope angle below a certain threshold. Also, in this case, the value is empirically based on the visual pattern and back analysis (slope distribution of ML). Then, all the raster values equal to one are converted into PL polygons. Additional filters may be introduced based on radiometric or geometric parameters. These filters based on empirical thresholds should be

205   evaluated case by case considering the morphology, the land use and the ancillary data available in the study area. We finally obtained the final PL inventory with their centroid.

We used the PL centroid to create with QGIS a Kernel heatmap relative density (KD) map of relative PL. The PL KD aims to identify the most affected area. The parameters used to generate KD maps (e.g. search radius) depend on the dimension of the study area and the average distance of PL centroids. The same procedure is applied to the ML to create

210   a density map for inventory comparison.

3.1.4 Parameters iteration based on ML inventory comparison

The first PL inventory is then compared with a ML drawn on high-resolution images in a limited subarea of the AOI. The

215   manual mapping is done on a small training area (e.g. 10 % of the whole AOI), and it is used as a benchmark dataset for calibrating the proposed method.

The identification of the training area is based on the following criteria: i) availability of cost-free high-resolution post-event images, ii) PL density map, described in the previous paragraph, iii) intensity of the event (*e.g.,* accumulated rainfall), iv) representativity of the study area in terms of lands-use and geomorphology. Once the result of the training

220   area is available, it is possible to evaluate the statistical distribution of ML inventory in terms of $NDVI_{var}$, slope angle or other parameters for a better empirical calibration of the thresholds used to create the PL. The iteration step aims to reduce the false positive and false negative and obtain the definitive PL inventory.

Natural Hazards
and Earth System
Sciences
Discussions
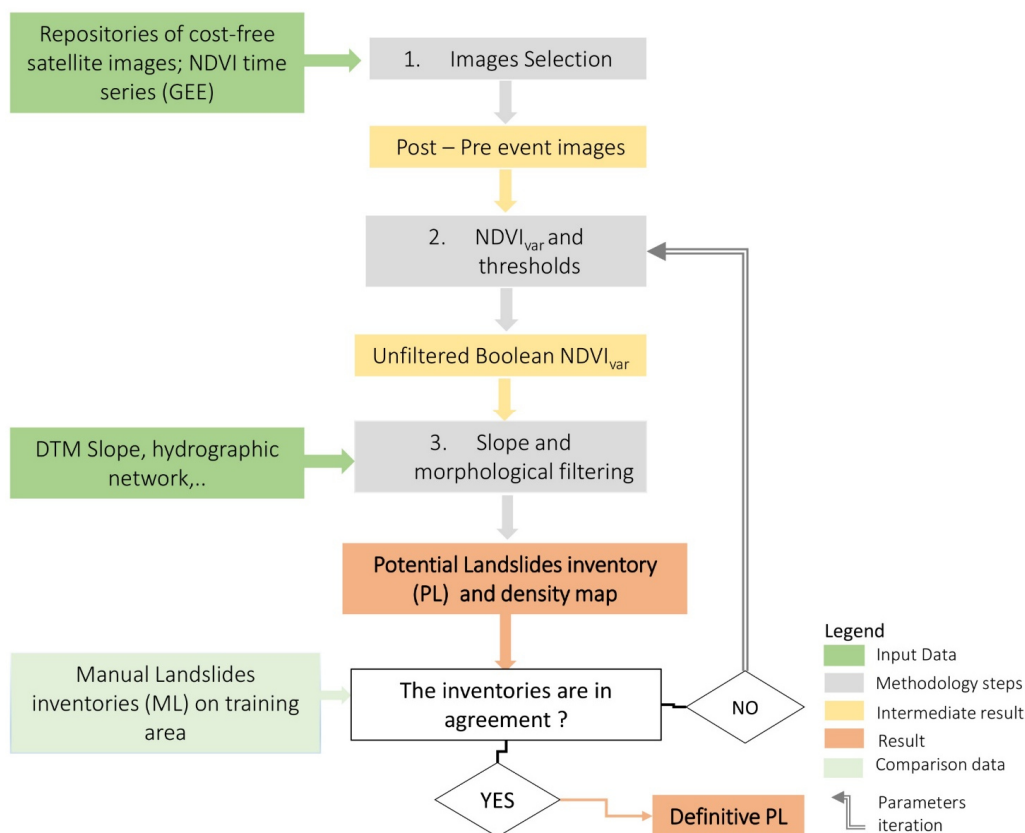
Figure 3. Flow chart of proposed shallow landslides mapping methodology.

225

3.2 Data, parameters and thresholds used for the case studies

We applied the methodology described above to our two case studies; for each, we chose the data and parameters described in the following paragraphs. The data availability section provides the link to the original databases used.

3.2.1 Satellite data and geomorphological filters

230   Following the methodology described in section 3.1, we first selected the pre- and post- images. For our case studies, we used the data of Sentinel-2 satellites (type Bottom-Of-Atmosphere reflectance in cartographic geometry - L2A) available on the Sentinel-Hub portal (Copernicus Open Access Hub, 2022). In particular, we downloaded the 10-m resolution bands visible (B2, B3, B4) and near-infrared (NIR - B8), and we clipped the original datasets on the area of interest. The dataset used in this study are listed in Table 1. For the Gavi area, we find a pair of images with one year of interval, while for

235   Tanarello and Arroscia valley area, the best pair cloud-free is on two years interval.

In the second step, we defined the NDVIvar and geomorphological thresholds. In our case study, we used $NDVI_{VAR} \leq -0.15$ joined to slope$> 15°$ entries values to create the Boolean raster where the value 1 identifies the potential landslides. The slope models were computed from 5-m DTM available from the databases of Piemonte and Liguria regions. The boolean raster keeps the same spatial resolution of Sentinel-2 (10x10 m pixel).

240 We used additional geomorphological thresholds such as the median slope of the PL polygons. The values were based on the statistical distribution of ML median slope. We used the filter values median slope >= 17° and >= 20° for the Tanarello and Arroscia valley area and the Gavi area, respectively.

In the Tanarello and Arroscia valleys case, we removed the polygons nearby (using an empiric buffer from 5 to 10 m) the hydrographic network to remove false positives related to riverbank erosion. We also filtered the areas in a constant

245 shadow because of a cliff, using threshold values of the averaged means of the four 10-m bands (RGB and NIR) of Sentinel-2 images. The PL polygons were finally smoothed and merged if their distance was lower than 1 m.

Table 1: Sentinel-2 images used in the selected case studies

Case study	Image Source	Band	Spatial resolution	Pre-Event images	Post-Event Images	Usage
Tanarello and Arroscia valleys	Sentinel-2	R-G-B; NIR	10 m	23/08/2016	28/08/2018	Semi-Automatic detection
	GEE	NDVI	10 m	2016-2021		NDVI time series
Gavi area	Sentinel-2	R-G-B; NIR	10 m	26/06/2019	20/06/2020	Semi-Automatic detection
	GEE	NDVI	10 m	2016-2021		NDVI time series

250 **3.2.2 High-resolution images for ML inventory.**

Concerning the Gavi area case study, we focus the manual mapping over small training areas (about 50 km^2), this allows tuning the parameters to produce the PL over the whole study area (552 km^2). For the Tanarello and Arroscia valleys case study, the ML training area corresponds to the entire study area because we decided to test the iteration step with more

255 detail and obtain a complete semi-automatic inventory validation.

The manual mapping of the landslides was made on very high-resolution post-event images. In our case study, high-resolution images were available for both areas, dating back to a few months after the events (Table 2). We used the post-event satellite images available on Google Earth upload as XYZ tiles layer on QGIS software. We also used pre-event high-resolution orthoimages available as a web map service (WMS) on the national cartographic service of Italy or the

260 regional web map service of Piemonte and Liguria regions.

The manual polygons of landslides (ML) were drawn following geomorphological criteria with the help of shaded relief DTM. Two operators manually checked the inventories to reduce the subjectivity of mapping. The landslide mapping was made on QGIS with the support of Google Earth Pro for historical image visualisation.

265 **Table 2. High-resolution images used for ML mapping in this work.**

Case study	Image Source	Band	Spatial resolution	Pre-Event images	Post-Event Images	Usage
Tanarello and Arroscia valleys	Google Earth; National cartographic portal (PCN)	Visible	0.3 m	24/09/15 2012	03/08/17	PL Validation and Manual mapping
Gavi area	Google Earth; Piemonte regional webgis service	Visible	0.3 m	01/06/2019 2018	07/04/2020 16/03/2021	PL Validation

Natural Hazards
and Earth System
Sciences

Discussions

3.2.3 NDVI time series analysis using GEE.

270 We also used GEE's potentiality to check and compare the NDVI time series affected by shallow landslides. We manually draw on the GEE interface some sample polygons, imported as feature collections representative of different conditions (landslide / no landslides) and land use. As for the choice of the best images described in section 3.1, we used an algorithm based on (Nowak et al., 2021). We also extract the NDVI time series using the GEE time-series explorer QGIS plugin (GEE Timeseries Explorer), such script allows producing single-pixel TS directly from a point vector. The time series analysis is aimed to estimate the recovery of vegetation in the area affected by shallow landslides and compare it with
275 healthy areas. The NDVI time series located in different land use were also compared using GEE.

3.3 PL and ML inventories comparison and statistics

We compared the PL with ML to evaluate the efficiency of semi-automatic detection by using geoprocessing tools in a GIS environment. Results were synthesized in a validation matrix (Table 3). PL and ML vector layers were merged in a unique one to obtain the intersections between the two datasets, thus getting true positive (TP), then by selecting residuals
280 PL (i.e. parts non included in the intersection) touching or not the intersection, partial positive (PP) and false positive (FP) were detected. On the other hand, partial detection (PD) and false negative (FN) were defined, respectively, by residual ML touching the intersection sector and ML not intersected with PL. The five categories were merged in a unique vector layer for further analysis, with the aforementioned classification stored in the attribute table.

The three types of intersections in which PL are involved (TP, PP and FP) were used to analyze and validate the semi-
285 automatic methodology. Then, by overlaying them on NDVI and slope angle raster layer, mean values were calculated and stored for each feature. Those values were then processed to obtain descriptive statistics and frequency distributions in terms of the previously described categories. The ML/PL comparison of datasets was also used in an iteration process to enhance the parameters to obtain the PL. The characteristics of FP allowed improving the filters in semi-automatic detection. We use the false-positive ratio (FPR, equation 2) to measure the percentage of the area not correctly

290 $$detected FPR = (FP) / [(FP) + (TP) + (PP)] (2)$$

We define the detection ratio (DR, equation 3) to evaluate the efficiency of our methodology: The DR measures the percentage of shallow landslides detected by the PL methodology. We also analyse the factors influencing the DR, such as shallow landslide dimension or land use.

295 $$DR = [(TP) + (PD)] / [(TP) + (PD) + (FN)] (3)$$

Table 3. Inventories comparison matrix

Intersection type	Denomination
Area of the full intersection of PL and ML	True Positive (TP)
PL intersected by ML but not overlapping	Partial Positive (PP)
ML intersected by PL but not overlapping	Partial Detection (PD)
Detected by PL not Mapped in ML	False positive (FP)
Not Detected by PL and Mapped in ML	False negative (FN)

We also compare the PL and ML inventories using the KD maps made with the procedure described in paragraph 3.1.3.
300   The two densities, sampled on the same regular grid, are compared in a scatter plot, and a correlation coefficient is
calculated (Benesty et al., 2009).

4. Results and discussion

The proposed methodology was applied to the two case studies of the Tanarello and Arroscia valleys (2016) and the Gavi
area (2019). We obtained for both areas PL and ML inventories with more than 1000 shallow landslides mapped for each
305   AOIs. The comparison of ML and PL inventories allowed us to compute statistics on the semi-automatic mapping
approach's efficiency and improve parameters with iteration. We used the NDVI time series computed on GEE to evaluate
the post-event vegetation recovery. Finally, a comparison with other ancillary datasets was made to analyse shallow
landslide distribution characteristics. In the supplementary material, two figures show an example of the application of
our methodology step-by-step for the sampled area of the two case studies

310   ### 4.1 Tanarello and Arroscia valleys study area

The semi-automatic mapping based on $NDVI_{var}$ of pre-event (2016-08-23) and post-event (2018-08-28) Sentinel-2
images, for the Tanarello and Arroscia valleys study area provided 1056 PL.

Figure 4 shows an example of the steps and results of our methodology over a sample area of the Arroscia/Tanerello case
study. From the comparison of pre- (Figure 4 A), and post-event images (Figure 4 B), we obtained the $NDVI_{var}$ that was
315   used to extrapolate the PL (Figure 4 C). Figure 4 D compares the ML draw on high-resolution Google Earth satellite
images and the PL. A detailed 3-D view from Google Earth Pro of pre- and post-event is shown in Figures 4 E and F.
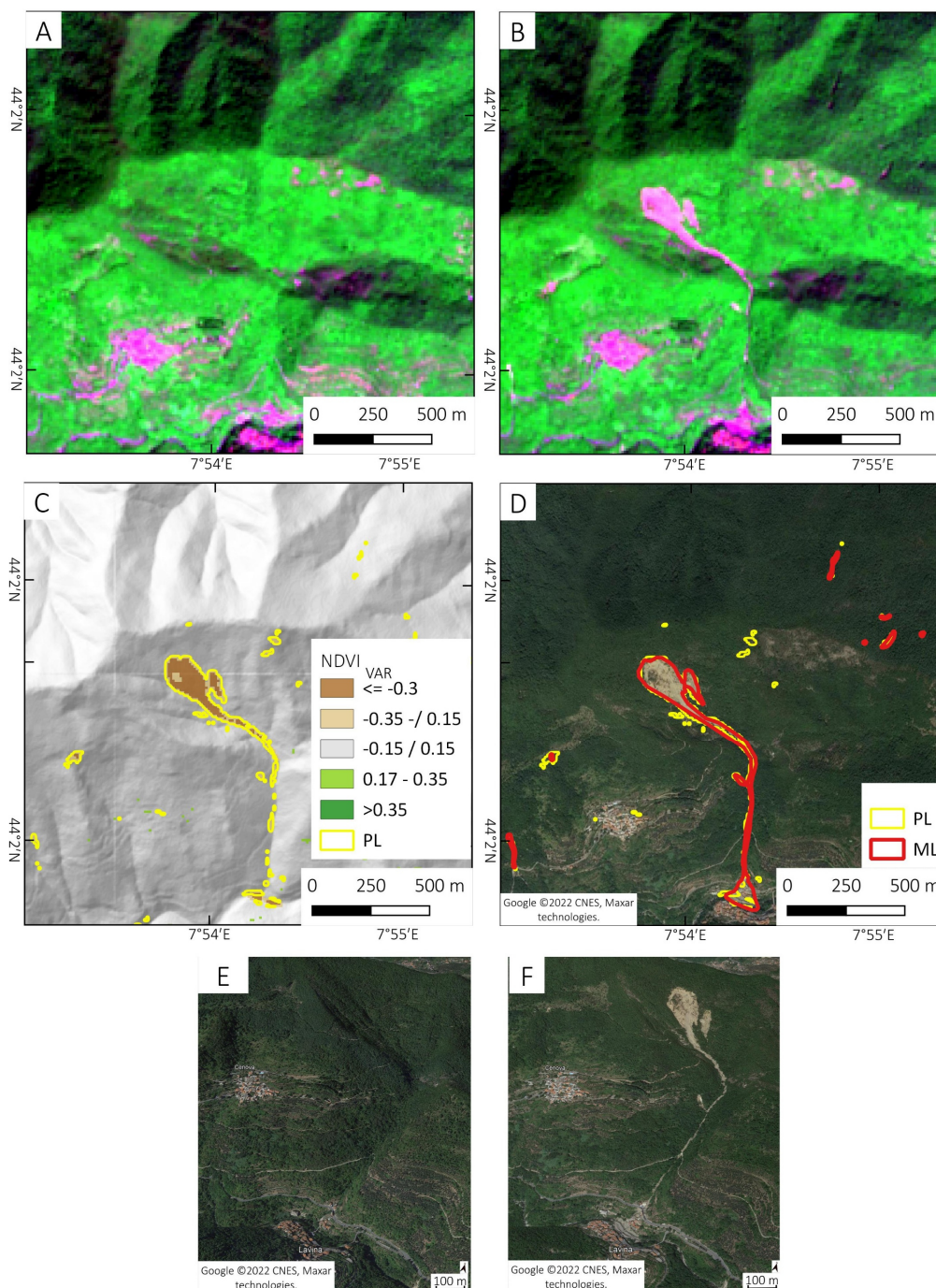
Figure 4. Example of shallow landslides detection methodology for Tanarello and Arroscia valleys case study: A) Sentinel-2 pre-event images (RED-NIR-BLUE) acquired on 2016-08-23; B) A) Sentinel-2 post-event images (RED-NIR-BLUE) acquired on 2018-08-28; C) NDVI$_{var}$ map PL inventory; D) ML and PL inventory overlapped to post-event high-resolution image (Google Earth – 2017). Google Earth 3D view of pre- (E) and post- (F) events of the area affected by landslides. Maps data: Google ©2022 CNES, Maxar technologies.

320

4.1.1 PL density and distribution

325

The distribution and Kernel density (KD) (search radius 1000 m) of PL centroids are shown in Figure 5 A. At the basin scale, it is possible to appreciate a high density of PL in the central sector, particularly in the Arroscia, Armetta and Tanarello valleys, where the density reaches a peak of 10 centroids / km². Moreover, Figure 5 B shows a PL detail

330 corresponding to riverbank erosion, not filtered because the hydrographic network has no precise geocoding. It is challenging to create an affordable geomorphological filter discriminating river erosion from a shallow landslide in a steep valley, and in many cases, the two processing overlap or are linked by a cause-effect relationship. Figure 5 C shows the correct detection of a landslide, its shape is almost accurate considering the Sentinel-2 resolution, while Figure 5 D shows a shallow landslide not detected (false negative case) because the shadow mask filters it out.
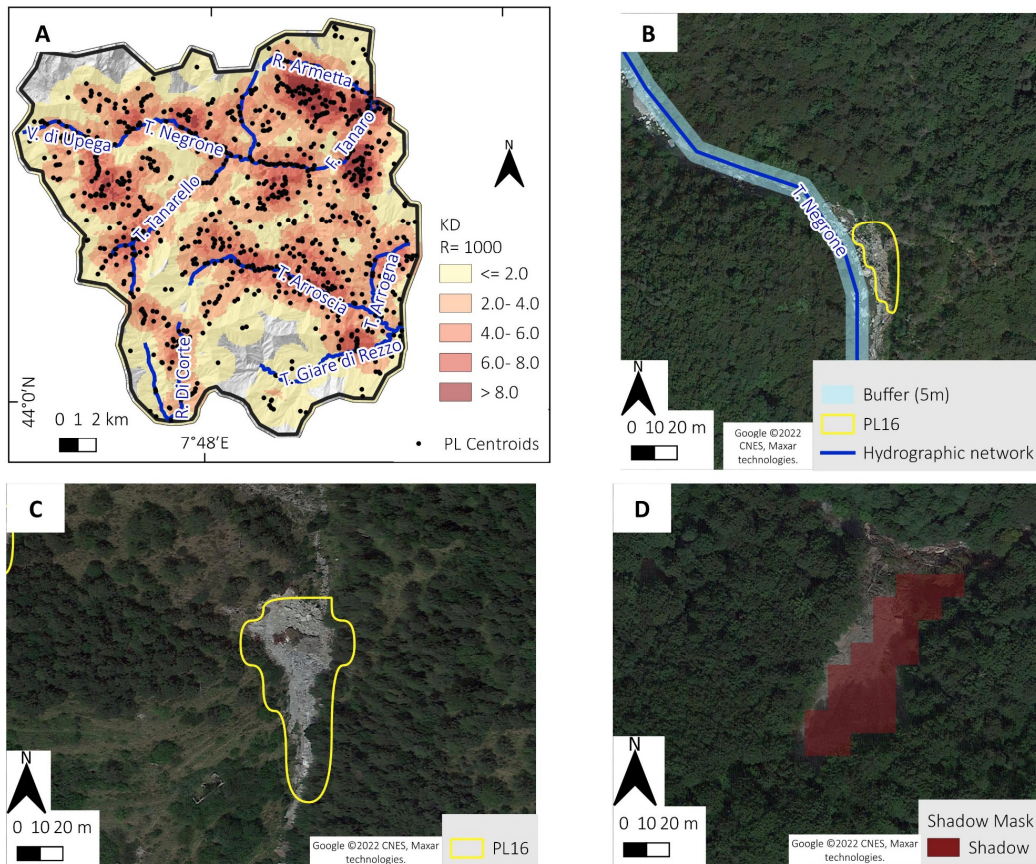
335

Figure 5. A) The Kernel landslides centroids relative density (search radius = 2500). **B)** Detail of PL representing a river bank erosion; **C)** PL that correctly detects the shallow landslide, **D)** Shallow landslides not detected by PL because filtered with a shadow mask. Maps data: Google ©2022 CNES, Maxar technologies. Hillshade and of map A is based on 5-m DTMs of ARPA Piemonte and regione Liguria.

340

4.1.2 PL and ML comparison statistics.

345 The manual mapping of landslides made on post-event Google Earth and high-resolution satellite images was compared with pre-event aerial photos of 2012 and allowed the detection of 1098 ML (average density 3 ML/km²).

The intersection of ML and PL inventories allowed the calculation of several statistics on detection capability and the evaluation of the semi-automatic detection parameters. Figure 6 A shows, over a sample area, some examples of the intersection of PL and ML inventories. In Figure 6 B, the intersections are classified into the five types of combinations defined in Table 3. In some cases, the PL/ML overlapping (TP) is almost complete (intersection 1) in Figure 6 A and B,

350 while in other (intersection 2), TP represent a small portion of the intersection. For the whole Tanarello and Arroscia valleys case study, we also reported the intersection cases pie charts by polygons count (Figure 6 C) and area (Figure 6 D).

The detailed validation results for PL made with R (see section 3.3) are shown in Figure 7. The chart of Figure 7 A shows the number distribution of TP, PP and FP cases. The TP represents about 32 % of intersected PL summed with the PP,

355 representing 29 % of intersections, showing that the methodology detects a shallow landslide in 60 % of cases. The area frequency distribution chart (Figure 7 B) indicates that the PP cases have smaller areas (median 165 m^2) than TP (230 m^2) cases, this means that the TP increase up to 38 % of the case considering the area sum instead of polygons count. Several FP cases correspond to fluvial processing like bank erosion that filters could not remove. Some other regions correspond to artificial forest cuts that occurred from 2016 to 2018. In addition, the only complete summer cloud-free

360 pair of images is august 2016 vs august 2018, and this extended period increased the probability of detecting land-use change.

The NDVI$_{var}$ and the slope are the main parameters used to detect landslides, therefore, their distribution inside the intersected PL-ML inventories helped to understand the efficiency of the semi-automatic approach. Figure 7 C shows the median NDVI$_{var}$ for each class of ML-PL intersections. The TP cases show NDVI$_{var}$ values below the -0.16 threshold,

365 probably because the shallow landslides strongly impact vegetation compared to other land-use changes. Figure 7 D shows the median slope distribution, in this case, there are few differences among the classes because the slope filter (17°) removed most FP related to slope gradient. This means that most FP are caused by a land-use change or riverbank erosion with the same slope gradient of shallow landslides.

370
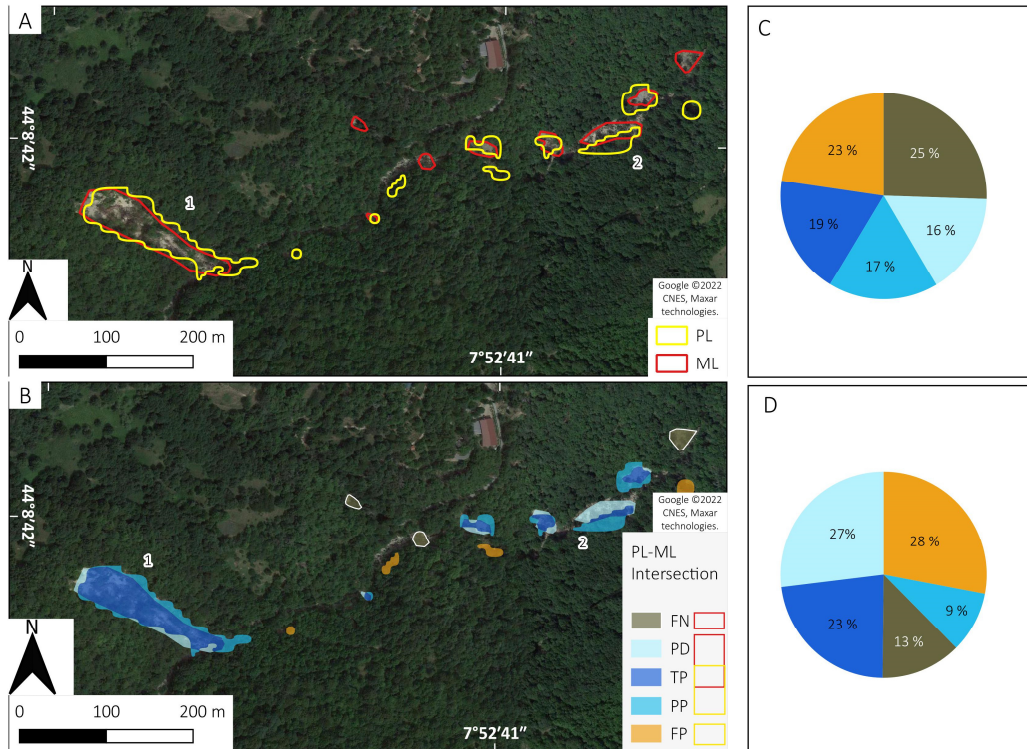
Figure 6. Tanarello and Arroscia valleys case study. A) PL-ML inventories intersections over a sample area. B) PL-ML intersection classified by type. Pie charts of the intersection type distribution by number (C) and area (D). Maps data: Google ©2022 CNES, Maxar technologies.

375
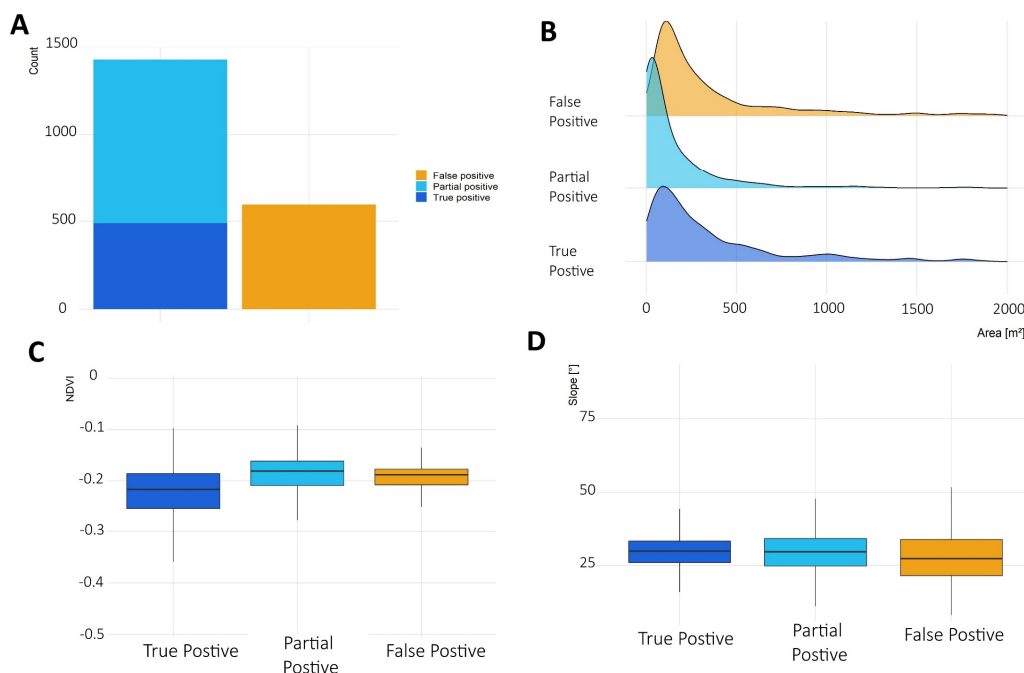
Figure 7. PL validation statistics for the Tanarello and Arroscia valleys case study: A) Bar plot showing the number of polygons of PL classified as TP, PP and FP area; B) Area frequency distribution for the polygons classified as TP, PP, and FP area C) Box plot chart of NDVI$_{var}$ distribution for TP, PP and FP classes ; D) Box plot chart of median slope distribution for each class of ML-PL intersection.

4.2 Gavi area case study.

For the Gavi area case study, we used the Sentinel-2 2019-06-20 (pre-event) and 2020-06-26 (post-event) images. The semi-automatic mapping allowed us to obtain about 3100 PL and 1077 of them are inside the training area.

Figure 8 shows an example of the steps and results of our methodology over a sample area of the Gavi 2019 case study. From the comparison of pre- (Figure 8 A), and post-event images (Figure 8 B), we obtained the NDVI$_{var}$ that was used to extrapolate the PL (Figure 8 C). Figure 4 D compares the ML draw on high-resolution Google Earth satellite images and the PL. A detailed 3-D view from Google Earth Pro of pre- and post-event is shown in Figure 8 E and F.
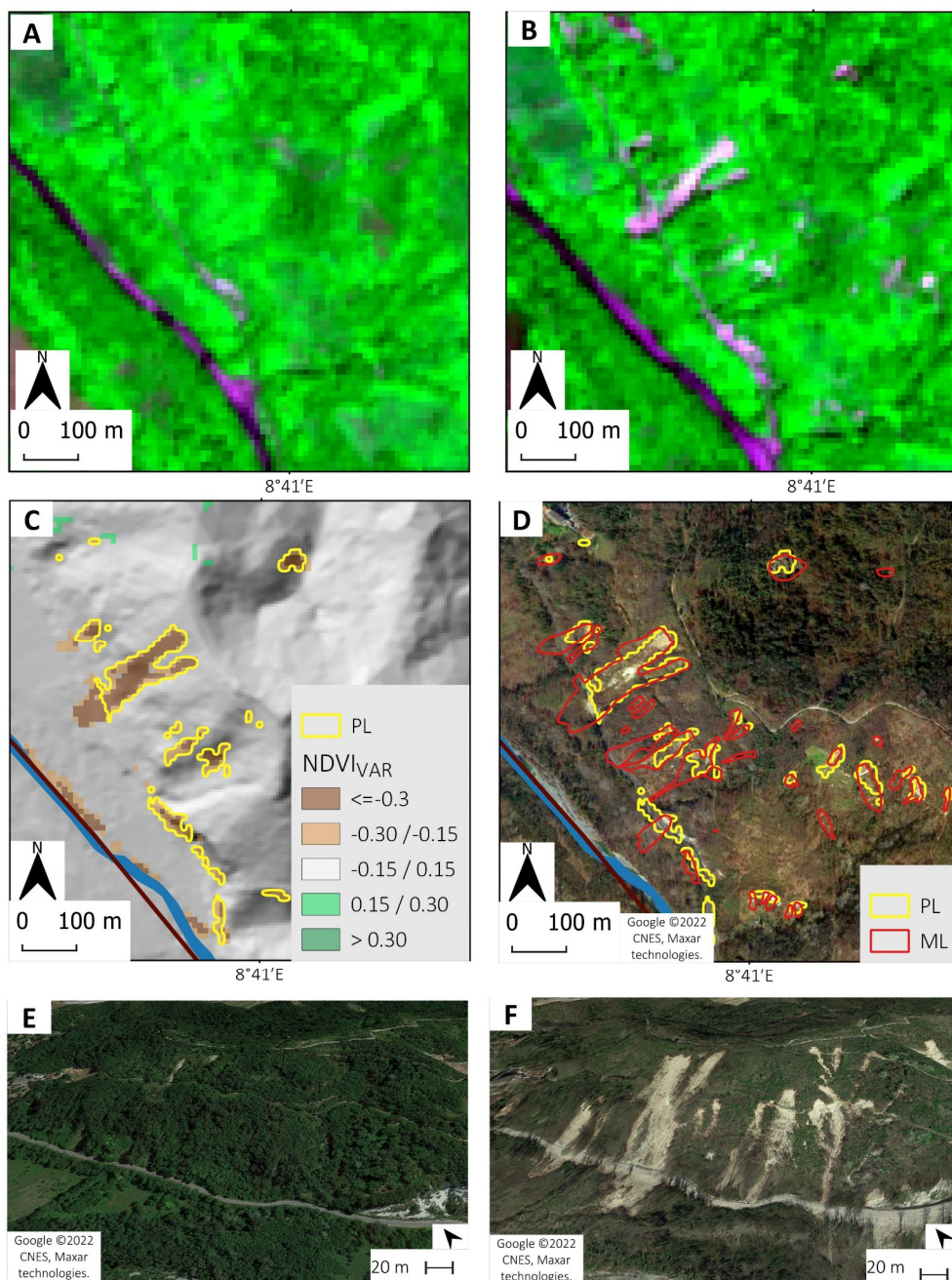
390   **Figure 8.** Example of shallow landslides detection methodology for Gavi 2019 case: A) Sentinel-2 pre-event images (RED-NIR-BLUE) acquired on 2019-06-20; B) A) Sentinel-2 pre-event images (RED-NIR-BLUE) acquired on 2020-06-26; C) $NDVI_{var}$ map and PL polygons; D) Comparison of ML and PL inventories overlapped to Google-Earth post-event image. Google Earth 3D view of pre- (E) and post- (F) events of the area affected by landslides. Maps data: Google ©2022 CNES, Maxar technologies.

395

4.2.1 PL density and distribution

Figure 9 shows the Kernel centroids density (based on a search radius of 1000 m) and distributions for PL inventory (Figure 9 A). About 3000 PLs were identified using the parameters and the filters described in the methodology section,

400   1100 of them are inside the training area. It is possible to detect an area of higher density chosen as a training area for manual mapping. Another area of high PL density is North of Ovada town and other minor areas South of Acqui Terme. It is possible to analyze the different cases of PL methodology results in more detail. Figure 9 B shows the correct detection of a landslide, its shape is almost accurate considering the Sentinel-2 resolution. Figure 9 C show a PL that partly detected shallow landslides: in many cases, the trigger points are detected because of their abrupt changes, while

405   the bottom part with more shallow sediment flow is not detected. It is also possible to appreciate two small shallow landslides not caught on Sentinel-2 images. Figure 9 D shows a false positive case where PL most probably detected a change in vegetation activity within a vineyard.
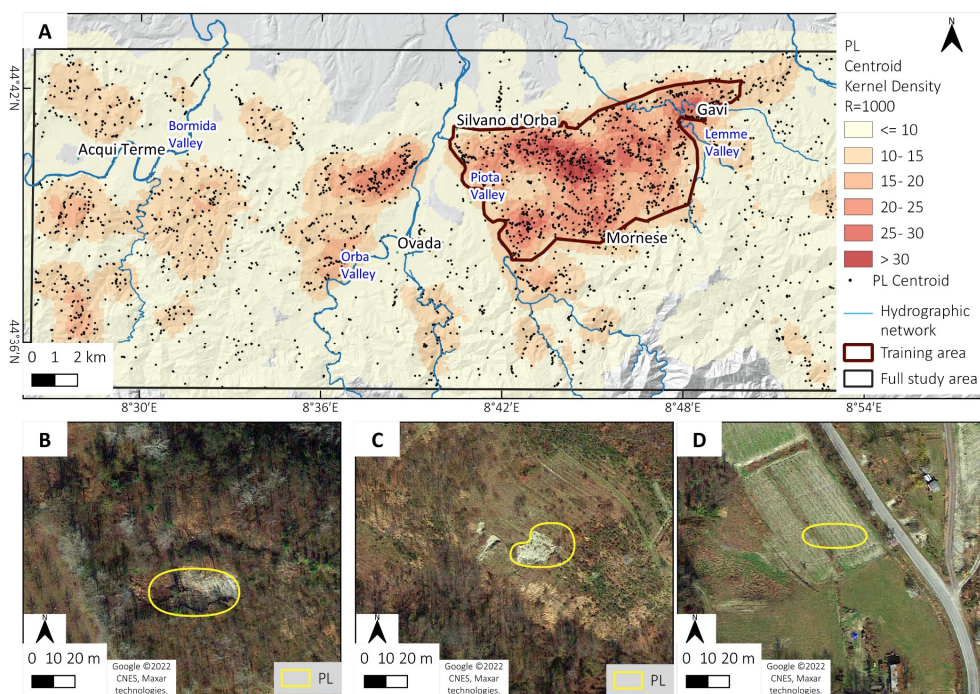
Figure 9. October 2019 event. A) PL centroids relative Kernel Density (R=1000) over the whole AOI. Some examples of PL:
410   **B) PL that completely overlaps a shallow landslide; C) PL that partly overlaps a shallow landslide; D) PL that corresponds to a false-positive case. Maps data: Google ©2022 CNES, Maxar technologies. Hillshade and of map A is based on 5-m DTM of ARPA Piemonte.**

4.2.2 PL and ML comparison statistics.

415

Also, for the Gavi area case study, we made similar statistics on inventories intersection used for the Tanarello and Arroscia valleys case study. The manual mapping of landslides, made on post-event Google Earth, and high-resolution satellite images compared with pre-event aerial photos of 2018, resulted in 1178 ML (average density 23 ML/ km^2).

Figure 6 A shows, over a sample area, some examples of the intersection of PL and ML inventories. In Figure 10 B, the
420   intersections are classified into the five types of combinations (TP, FP, FN, PD and PP) defined in Table 3. In some cases,
the PL/ML overlapping (TP) is almost complete (case 1) or partial (case 2). In other cases (3) the PL allowed to detect
only a tiny portion of the intersection, and most of the shallow landslide area was classified as PD. For the whole 2019
study area, we also represented the intersection cases pie charts by polygons count (Figure 10 C) and area (Figure 6 D)

The detailed validation statistics results for PL made with R (see section 3.3) are shown in Figure 11. The chart of Figure
425   11 A shows the number distribution of TP, PP and FP cases. The TP represents about 43 % of intersected PL summed
with the PP, representing 37 % of cases, showing that the methodology detects a shallow landslide in 80 % of cases. The
results of semi-automatic mapping for Gavi AOI are better than Arrocia-Tanarello AOI. The better performances could
be explained by a better pair of pre- post- images and the stronger magnitude of the 2019 event. The area frequency
distribution chart (Figure 11 B) shows that the partial positive cases have smaller areas (median 165 m^2) than TP (230
430   m^2), this implies that the percentage of TP rise from 43% to 49 % of PL considering the area sum instead of polygons
count. FP cases generally correspond to changes in agriculture activity in the vineyard that occurred in 2019-2020. As
previously stated, NDVI$_{var}$ and slope were analysed in terms of intersection class and provided the same insight concerning
the influence of vegetation health and acclivity.
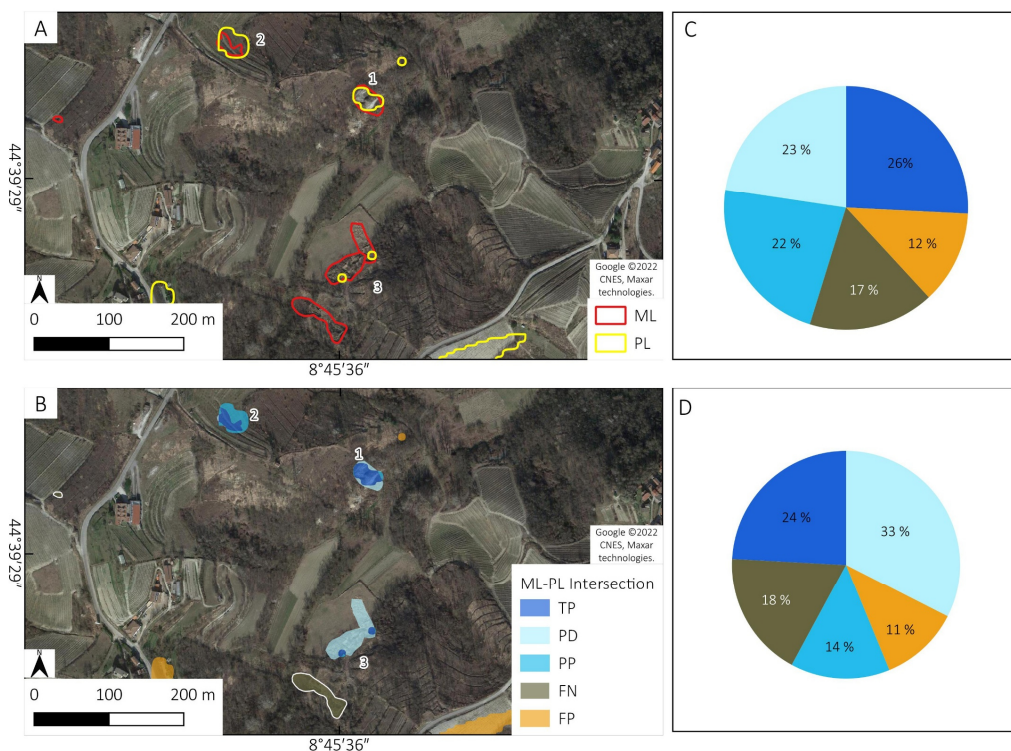
435   **Figure 10. 2019 Gavi case study. A) PL-ML inventories intersections over a sample area. B) PL-ML intersection classified by
type. Pie charts of the intersection type distribution by number (C) and area (D). Maps data: Google ©2022 CNES, Maxar
technologies.**
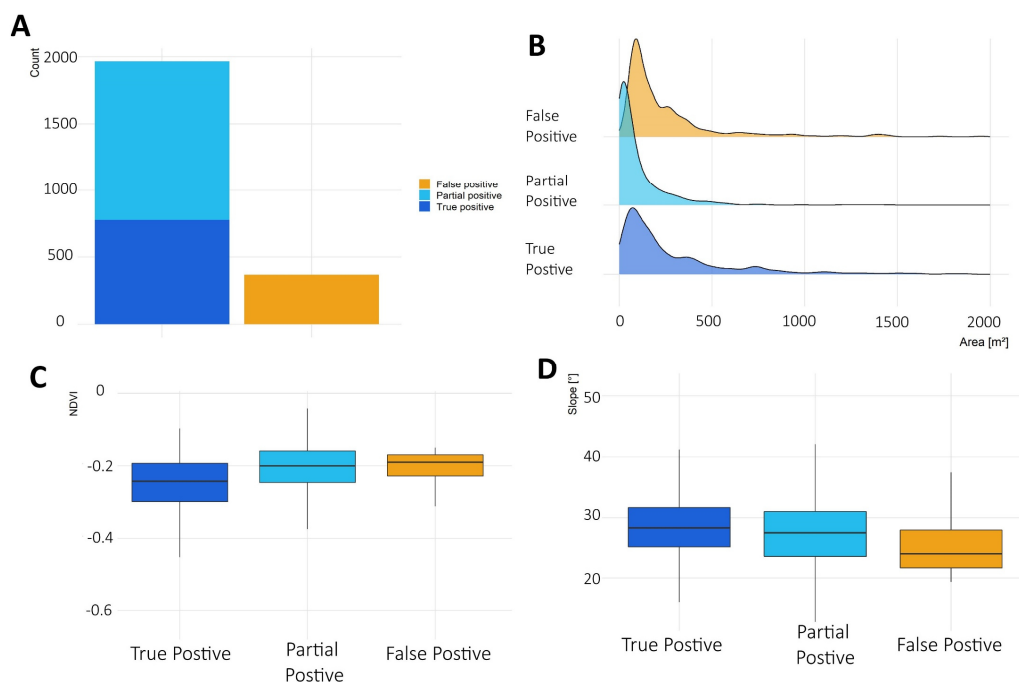
440 **Figure 11. PL validation statistics for the 2019 Gavi study area: A) Bar plot showing the number of polygons of PL classified as TP, PP and FP area; B) Area frequency distribution for the polygons classified as TP, PP, and FP area C) Box plot chart of NDVIvar distribution for TP, PP and FP classes ; D) Box plot chart of median slope distribution for each class of ML-PL intersection.**

445 **4.3. Factor that influences shallow landslides detection and false positive.**

In this chapter, we discuss the main factors that, according to our results, influence the efficiency of the proposed PL methodology. As already treated in the literature, the landslide size (Bellugi et al., 2021; Fiorucci et al., 2018), land use (Mondini et al., 2011) and the temporal interval (Lindsay et al., 2022; Scheip and Wegmann, 2021) used in the pre- post-event calculation seem the most interesting to discuss on the base of our results

450 **4.3.1 Shallow landslide size, density and distributions.**

The detection capacity is mainly related to shallow landslides size and spatial resolution of Sentinel-2.

Figure 12 A and B show the histogram distribution of ML size for the Tanarello and Arroscia valleys and Gavi study areas, respectively. ML size distribution agrees with the classical power-law distribution of shallow landslides (Bellugi et al., 2021; Guzzetti et al., 2002) for both cases study. This means that the shallow landslides smaller than 500 m^2 are

455 about 60% of all ML inventories, but they represent only 20 % of the total area affected. The histograms also show that for the Tanarello and Arroscia valleys (Figure 12 A), the MLs are generally smaller than in the Gavi area. The red bars show the ML intersected by PL (TP+PD intersection cases), it is possible to note the lack of distribution of small landslides, in agreement with the area frequency distribution for TP and PD cases shown in the Figure 7 B and Figure 11 B.

460   Figure 12 C and D show the DR calculated with equation 2 for the Tanarello and Arroscia valleys and Gavi study areas. The DR increases with the size of the landslides, and it is strictly related to the pixel size of Sentinel-2. For the landslides smaller than 100 m^2 (Sentinel-2 spatial resolution) the DR range from 10% of Tanarello and Arroscia Valley (Figure 12 C) to 15 % in the Gavi area (Figure 12 D). It is clear that for these landslides, the Sentinel-2 platform is not the optimal choice (Fiorucci et al., 2018), and manual mapping on high-resolution images is better than semi-automatic mapping. On

465   the other hand, for the ML in the class area (500 – 1000, i.e., 5 – 10 pixels of a Sentinel-2 image), the DR range from 65 % of Tanarello and Arroscia Valley to 80 % of the Gavi area.

The overall DR considering polygons count is 39 % for the Tanarello and Arroscia Valley and 58 % for the Gavi case study, while considering the area sum, the DR is 60 % and 75%, respectively. The Gavi case study's better performance is likely related to the size distribution of shallow landslides and the better pair of images used to create PL.
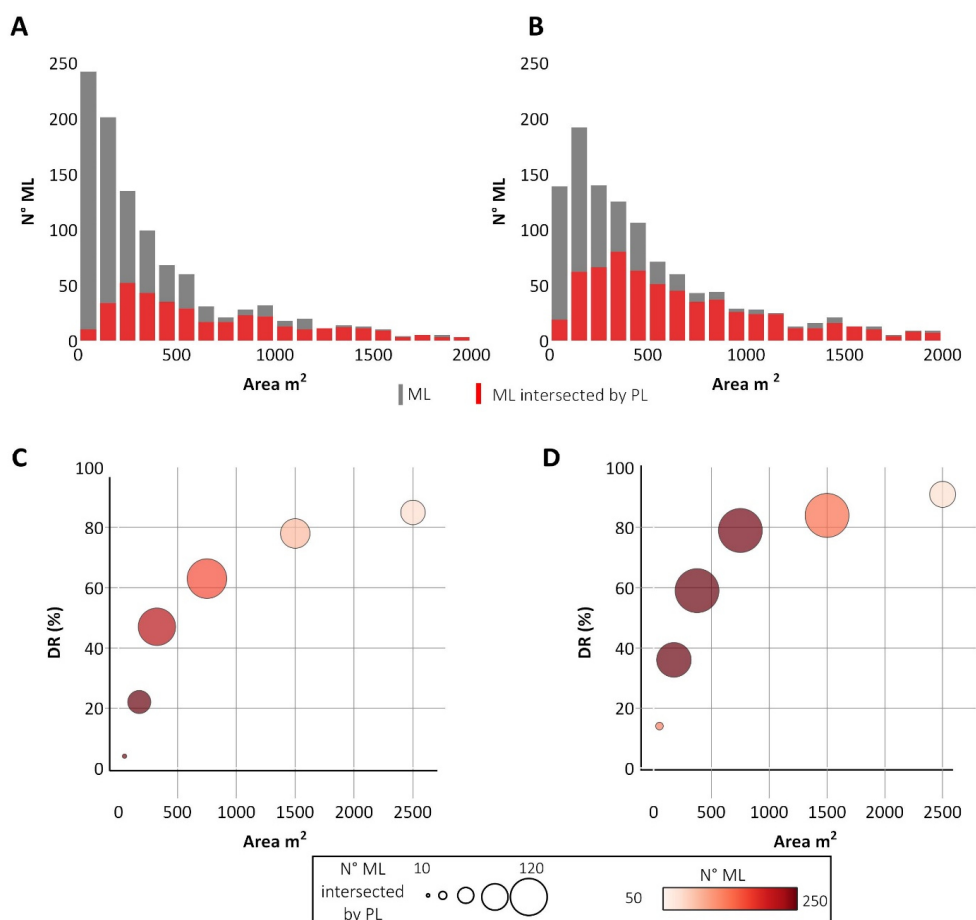
470

Figure 12 Histogram of ML area distribution for Tanarello and Arroscia valleys (A) and Gavi (B) study areas, the grey bars represent the entire ML inventory while the red one represents the ML intersected by a PL. Detection rate (DR) for each area class for Tanarello and Arroscia valleys (C) and Gavi area (D) case study. The size of the circle is correlated with the number of detected ML; the colour scale represents the total number of ML for each class.

475

Natural Hazards
and Earth System
Sciences
Discussions

The ML and PL density and distribution comparison agree with both the Tanarello and Arroscia valleys and Gavi area case studies. However, the differences described in the previous sections evidence that PL methodology performed better in the Gavi case study.

The results are also evident by comparing the distribution and density of PL and ML datasets. In the case of 2019, both ML and PL inventories, Figure 13 A and B show a higher density in the northern sector of the study area and a lower density in the central region. Figure 13 C shows the scatterplot between the PL and ML density, the correlation coefficient (Benesty et al., 2009) has a value of 0.85 with an $R^2= 0.73$ using a grid of 1000 m. Moreover, the average ML density is about 23 ML/km² higher than the 2016 event (3.1 ML/km²). The difference is probably related to the more intense rainfall of October 2019 (up to 500 mm in 24 h) compared to the 2016 case (700 mm in five days).

In the case of 2016, there are some more discrepancies. It is possible to appreciate a higher density of PL in the NE sector (Figure 13 D). At the same time, ML shows a density peak in the Arroscia valley (Figure 13 E). Both datasets show that centroids' high density is located in the central sector, particularly in the Arroscia, Armetta and Tanarello valleys, where the density reaches a peak of 10 centroids/km². At the basin scale, PL/ML regressions show a correlation coefficient of 0.68 with an $R^2= 0.47$ using a grid of 2500 m (Figure 13 F).
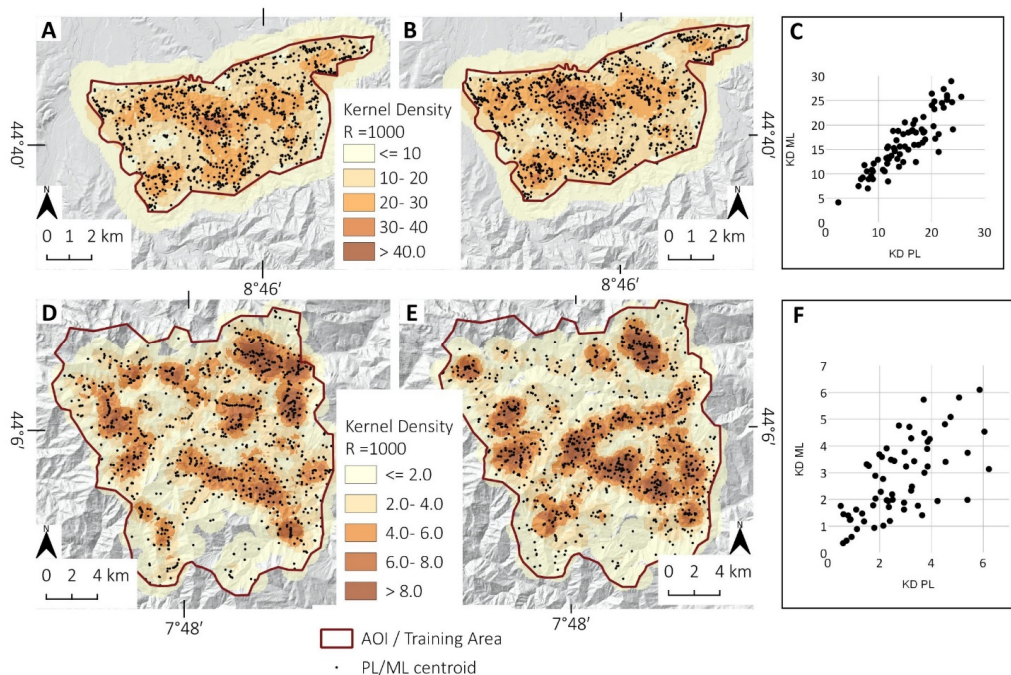
Figure 13. Heatmap Kernel Density for: A) Gavi PL inventory; B) Gavi ML inventory; D) Tanarello and Arroscia valleys PL inventory; E) Tanarello and Arroscia valleys PL ML inventory. Scatter plot of ML/PL Kernel density comparison for: D) Gavi training area; F) Tanarello and Arroscia valleys study area. Hillshade and of map A is based on 5-m DTMs of ARPA Piemonte and regione Liguria.

4.3.2 The effect of land use on PL methodology efficiency.

We deeply investigate the role of land use on landslides detection. The semi-automatic detection performed well for naturally vegetated slopes, while the detection capability decreased for cultivated landscapes.

22

Natural Hazards
and Earth System
Sciences
Discussions

500   For instance, the statistics on intersection cases for the main four land-use classes (Land Cover Piemonte, 2022) made
for the 2019 case study allowed us to understand the variable regarding land-use efficiency of semi-automatic mapping.

The forest and the new forested shrub areas (Figure 14 A and B) show a high percentage of TP cases, and about 80 % of
PL correspond to shallow landslides. Here, human disturbances are limited, and most NDVI$_{var}$ are related to landslides.
The FN (15% of the area) fits small landslides not detectable with Sentinel-2 because of its spatial resolution.

The vineyard land use (Figure 14 C) shows a high FP percentage (37%). In this land use, most FP are changes related to
505   vineyard management. FN are also higher (22%) compared to the forested areas. The cultivated land (Figure 14 D) shows
a high percentage of FN (30%). The underestimation can be explained by smaller landslide dimensions and the
agricultural practice that erases the signs of landslides.
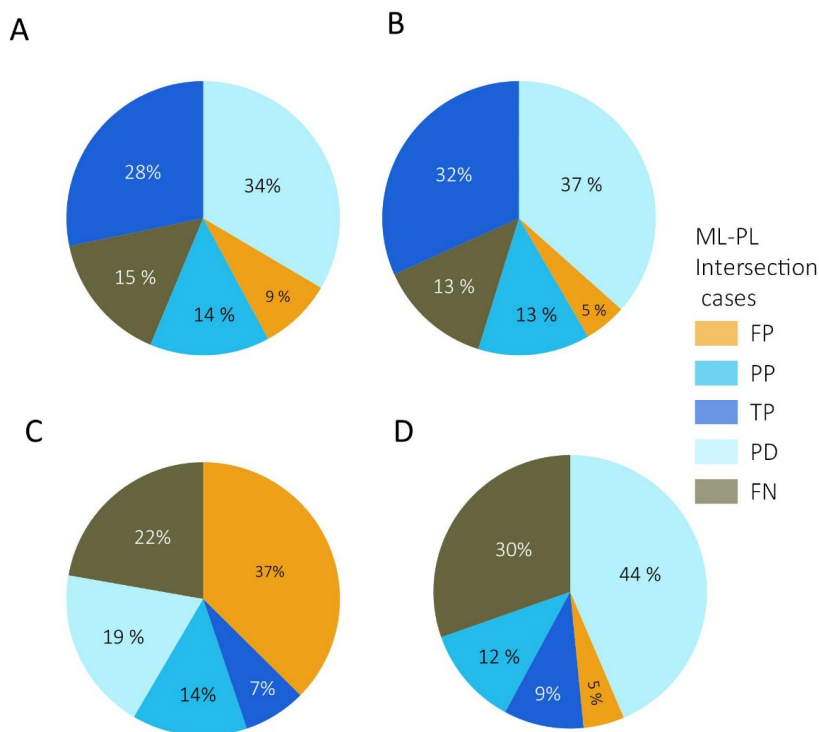
Figure 14. Gavi 2019 case study, PL-ML intersection distribution for the main land-use classes: A) Broad-Leaf forest; B)
510   **New-forest or shrubland; C) Vineyard; D) Cultivated land**

4.3.3 NDVI time series based on GEE

Figure 15 A and B show the NDVI time series based on Sentinel-2 computed on GEE (see data availability sections). The
515   NDVI time series of the area affected by shallow landslides (red line in Figure 15) is based on averaged NDVI of a subset
of ML polygons with an area of at least 500 m^2. This time series is compared with the averaged time series of a region

not affected by landslides (black line in Figure 15).

In the case of the Arroscia-Tanarello 2016 study area (Figure 15 A), it is possible to observe that in the areas not affected by landslides, the NDVI has a relatively constant seasonal trend during 2015-2021, ranging from 0.25 in winter to 0.75 in summer. On the contrary, the areas affected by shallow landslides showed a substantial decrease of NDVI (from 0.75 to 0.4) in the post-event 2017 summer. The NDVI slowly increased during the following years, up to the value of 0.55 in 2021. If we compare the pair images (2016-08-23, 2016-08-28) used to extract the PL, we can observe an average $NDVI_{var}$ of -0.2. Unfortunately, the summer 2017 images that show the best $NDVI_{var}$, are not fully cloud-free or acquired in the same seasonal period.

In the case of the Gavi case study (Figure 15B), in those areas not affected by landslides, the NDVI has a constant seasonal trend during the period 2016-2021, ranging from 0.2 in winter to 0.8 in summer. On the contrary, the NDVI of the area affected by shallow landslides shows a substantial decrease down to 0.6 from the summer of 2020. The NDVI value rebound to 0.65 in 2021. The pair images (2019-06-26, 2020-06-20) used to extract the PL show an average $NDVI_{var}$ of -0.15. The vegetation seems to recover faster compared to the 2016 case.

The effects of land use on detection capabilities are difficult to solve with simple filters, a partial solution could be the NDVI time series analysis. The analysis of the single-pixel time series of NDVI, generated with the GEE QGIS plugin (GEE Timeseries Explorer), allowed us to understand better the effect of landslide size and land use in the capacity detection of Sentinel-2, the main results are resumed in Figure 16.

Figure 16 A and A' show the location and the comparison of two NDVI time series in a broadleaf forest land use: the 1-p is entirely inside a ML of approximately 1500 m^2, while the 2-p is an undisturbed area. The two time series show almost the same seasonal trend until the 2019 event, after this, the NDVI of 1-p shows values of 0.2 less than the NDVI of 2-p in the 2020 summer.

Figure 16 B and B' show the location and the comparison for two single-pixel time series located in a vineyard land use. In this case, the (5-p) is situated in ML with an approximate size of 500 m^2 not detected by PL methodology (a false negative case). Both slide (5-p) and no-slide (6-p) NDVI time series show an irregular trend, probably related to the agricultural activity inside the vineyard. The post-event time series shows lower NDVI values for the pixel inside the ML, however, the noise is too high to extract a clear trend.

Figure 16 C and C' show the location and NDVI time series of a false-positive PL in a vineyard land use (9-p). In this case, the agricultural activity inside the vineyard caused a $NDVI_{var} < -0.16$ using the pre- and post-event pair images. However, if we look at the whole time series, there is no trace of the effect of shallow landslides.

Instead of considering single pre (2019-06-26) and post (2020-06-20) event dates, the noise could be reduced if we use averaged the pre- and post-event summer (May-September) images. Multi-temporal averaged satellite data on GEE have been already used to improve landslide detection (Lindsay et al., 2022). For instance, using this approach, the FP of Figure 16 C disappears because the $NDVI_{var}$ is -0.16 for single pairs while it is -0.03 for the averaged summer periods.

The summer averaged pre- and post-event NDVI computed with GEE for the Gavi area are available in the data availability sections.

Natural Hazards
and Earth System
Sciences
Open Access
EGU
Discussions
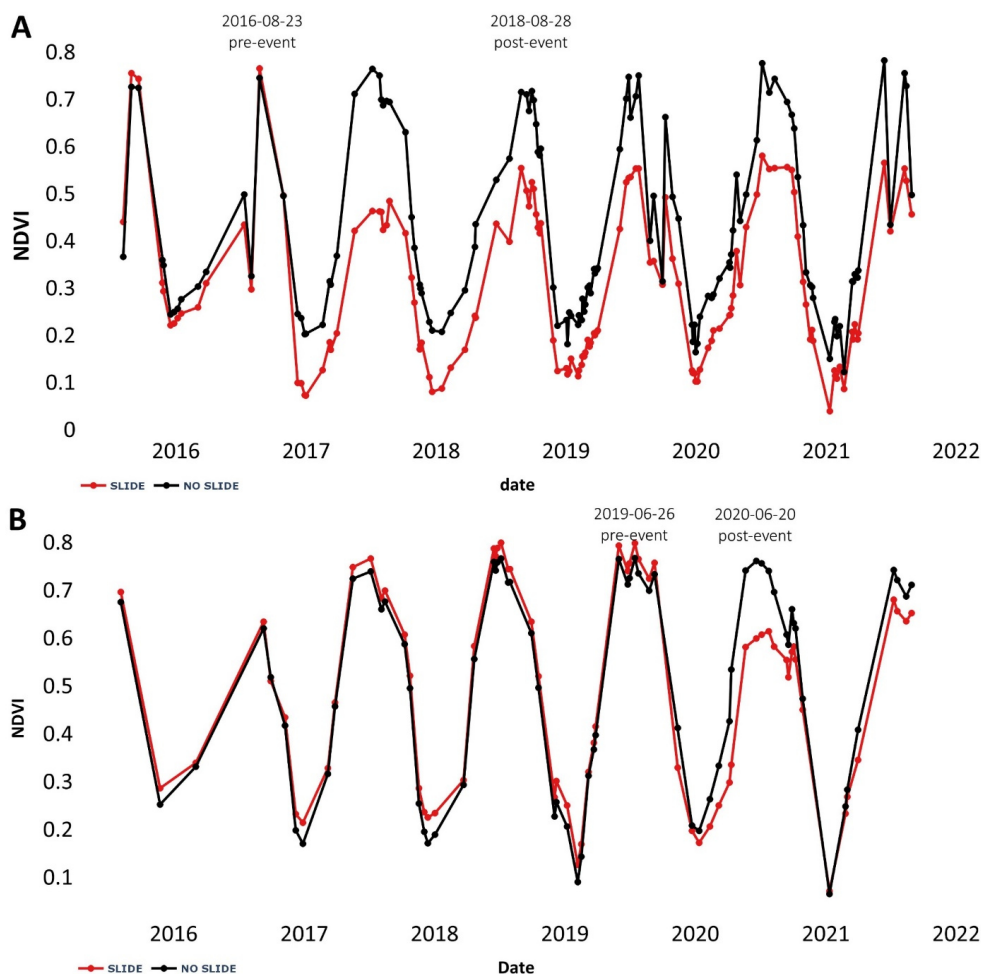
Figure 15. NDVI Time series based on Sentinel-2 data and processed with GEE: the 'Slides' red lines are the averaged time series of the selected ML; the 'no slides' black lines are the time series of the surrounding unaffected areas. A) 2016 Arrocia-Tanarello case study; B) 2019 Gavi case study.

555
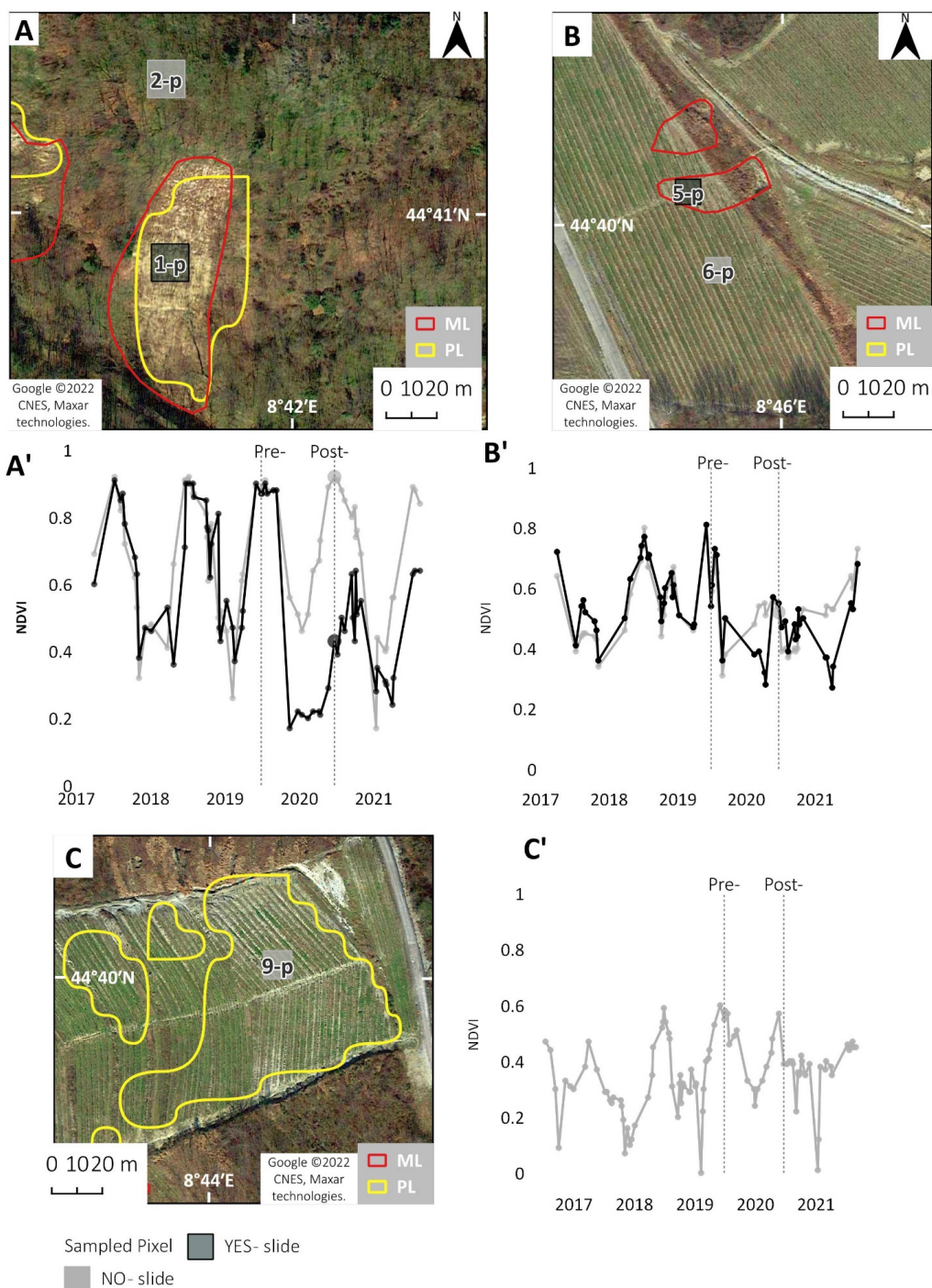
Figure 16. NDVI Time series (2017-2021 of five sample points (Landslide / No Landslide) in the area affected by the 2019 event. A and A' comparison located in a broadleaf forest (true positive); B and B' vineyard (false negative); C and C' vineyard (false positive). The Google Earth satellite image was acquired on 2021-03-16. Maps data: Google ©2022 CNES, Maxar technologies.

565 **6. Conclusions**

A low-cost semi-automatic methodology to detect shallow landslides using cost-free data from Sentinel-2 satellites, was implemented and tested in exemplary cases. The implemented user-friendly processing is aimed to be used by a wide range of final users, such as technicians or natural hazard planners with low expertise in remote sensing processing and computer science. Landslide data and GEE scripts were also available in free storage for the researcher and community

570 users. We tested the methodology on two extreme rainfall events that affected NW Italy in November 2016 (Tanerello and Arroscia valleys) and October 2019 (Gavi area).

We obtain a polygons dataset representing potential landslides (PL) and their density maps with the semi-automatic mapping. The PL density maps aim to identify the most affected areas, where to focus the manual mapping on high-resolution images. The PL dataset is created on three steps approach: i) choice of the best pair of Sentinel-2 images also

575 with the help of NDVI time series computed with Google Earth Engine (GEE); ii) creation $NDVI_{VAR}$ map from pre- and post-event images, iii) geomorphological filters based on slope and others parameters such as distance from the hydrographic network. In the study areas of Tanarello and Arroscia Valley, and Gavi, 1077 and 2576 PL were detected, respectively, and their density matches with most affected areas by rainfall events.

The dataset obtained was compared with manual mapping based on high-resolution images on training areas. We

580 manually map landslides on the free-cost high-resolution images (e.g., Google Earth, national or regional cartographic services). The manual mapping detected about 1100 ML over 300 km^2 in the Tanarello and Arroscia valleys and about 1180 ML over 55 km^2 in the Gavi area. The PL datasets were then compared with landslides manually (ML). The ML and PL inventories comparison shows a good agreement in density and distributions, especially for the Gavi case study.

The results show that a semi-automatic approach identifies the majority (> 60%) of shallow landslides larger than 2/3

585 Sentinel-2 ground pixel size (100 m^2), while only 20% of small landslides (< 100 m^2) are detected. In agreement with the power-law, small landslides are a high number, but a small fraction of the affected area. Consequently, the false-negative represents 60 % to 40 % of the cases but only 20-25 % of the area affected. In the future, using high-resolution cost-free satellite images for semi-automatic methods could drastically increase the detection capacity. Land use is another factor that influences detection capacity: in the Gavi study area, the detection rate reached 73 % on natural vegetation like forest

590 land use, while in cultivated areas, DR decreased up to 41 %,

The false-positive rate (FPR) (28 % for the Gavi area and 48% for Tanarello and Arroscia valley) is related to riverbank erosions or artificial change in vegetation pattern that was impossible to remove with geomorphological filters. Also, for FPR, the land use drives the performance: it ranges from 45 % of the vineyard to 20 % of the forest

The analysis of the NDVI time series with GEE was proper to identify the best pair of images and monitor the behaviour

595 of vegetation of affected areas. For the middle latitudes, the best comparison is with summer images. The time series showed a progressive vegetation recovery throughout the years, decreasing the detection capacity of this approach. The time-series analysis also suggested that an averaged NDVI of summer periods could reduce the effect of agricultural changes on vegetation and limit the false positive. The evidence indicated that multi-temporal analysis needs to be developed to improve semi-automatic mapping efficiency, which could be the key to future studies.

600

Data availability

ML and PL datasets used in this study are available in KML format on the Zenodo platform (Notti et al., 2022)

The Google Earth Engine scripts used for this paper are:

- NDVI Time series of some sampled areas to select the best pair of images for the PL creation (Tanarello and
605   Arroscia Valleys and GAVI AOIs (Fig. 15 of the manuscript) https://code.earthengine.google.com/8f4d08db4d34099bb1a4cd1fd15bf05b?noload=true

- Sampled NDVI Time series from different intersection cases for Tanarello and Arroscia Valleys study area https://code.earthengine.google.com/47e5883e0fe7beae589df4c42421dd3b?noload=true

- Sampled NDVI Time series from some test areas over the Gavi study area
610   https://code.earthengine.google.com/e97fd46102cca3ee25b441a8ebff8400?noload=true

- Multi-temporal averaged pre- and post-event NDVI for the whole Gavi study area https://code.earthengine.google.com/f773ed58fc39c201261c5e13b4275f97?noload=truem

The Sentinel-2 images were downloaded from Copernicus ESA open access hub website: https://scihub.copernicus.eu/

The High-resolution images were uploaded in QGIS as WMS layers from the following link:

615 - Google Earth Satellite layers, XYZ tiles for QGIS: http://mt0.google.com/vt/lyrs=s&hl=en&x={x}&y={y}&z={z}

- The 2012 Orthophots that cover both study areas are available on the national cartographic service (PCN) WMS: http://www.pcn.minambiente.it/mattm/servizio-wms/ Accessed: 2022-04-20

- The Piemonte region 2018 orthophoto is available on the following WMS:
620   https://opengis.csi.it/mp/regp_agea_2018?service=WMS&request=GetCapabilities&version=1.3.0, The Regione Liguria 2016 Orthophoto are available on http://www.cartografiarl.regione.liguria.it/mapserver/4.10/mapserv.exe?MAP=E:/Progetti/mapfiles/repertorioc artografico/ORTOFOTO/1828.map&VERSION=1.3 Accessed: 2022-04-20

DTM data can be dowload from Regione Piemonte and Liguria geo-portal:

625 - https://www.geoportale.piemonte.it/geonetwork/srv/api/records/r_piemon:224de2ac-023e-441c-9ae0-ea493b217a8e Accessed: 2022-06-30

- https://srvcarto.regione.liguria.it/geoviewer2/pages/apps/geoportale/index.html?id=2056 Italian) Accessed: 2022-06-30

The software Google Earth Pro was also used to map and check inventories at high resolution.

630 Other data, such as land use, NDVI elaborations and meteorological data, can be obtained from the first/corresponding author upon reasonable request.

Author contribution.

635 Planning and conceptualization were done by DN. Responsible for data curation were DN, MC, and DGo. The mapping was done by DN and MC. The statistical analyses were performed by DGo. The original manuscript was written by DN. MC, DGo and DGi were involved in reviewing and editing of the manuscript. Supervision and funding acquisition were provided by DGi.

Reference

640 ARPA Piemonte: Gli eventi alluvionali in Piemonte - Evento del 21-25 novembre 2016, Turin, 2018.

Bellugi, D. G., Milledge David G., Cuffey Kurt M., Dietrich William E., and Larsen Laurel G.: Controls on the size distributions of shallow landslides, Proceedings of the National Academy of Sciences, 118, e2021855118, https://doi.org/10.1073/pnas.2021855118, 2021.

Benesty, J., Chen, J., Huang, Y., and Cohen, I.: Pearson Correlation Coefficient, in: Noise Reduction in Speech

645 Processing, edited by: Cohen, I., Huang, Y., Chen, J., and Benesty, J., Springer Berlin Heidelberg, Berlin, Heidelberg, 1–4, https://doi.org/10.1007/978-3-642-00296-0_5, 2009.

Bordoni, M., Meisina, C., Valentino, R., Lu, N., Bittelli, M., and Chersich, S.: Hydrological factors affecting rainfall-induced shallow landslides: from the field monitoring to a simplified slope stability analysis, 193, 19–37, https://doi.org/10.1016/j.enggeo.2015.04.006, 2015.

650 Borrelli, L., Cofone, G., Coscarelli, R., and Gullà, G.: Shallow landslides triggered by consecutive rainfall events at Catanzaro strait (Calabria–Southern Italy), 11, 730–744, https://doi.org/10.1080/17445647.2014.943814, 2015.

Cardinali, M., Ardizzone, F., Galli, M., Guzzetti, F., and Reichenbach, P.: Landslides triggered by rapid snow melting: the December 1996–January 1997 event in Central Italy, in: Proceedings 1st Plinius Conference on Mediterranean Storms, 439–448, 2000.

655 Carrara, A.: Uncertainty in Evaluating Landslide Hazard and Risk, in: Prediction and Perception of Natural Hazards: Proceedings Symposium, 22–26 October 1990, Perugia, Italy, edited by: Nemec, J., Nigg, J. M., and Siccardi, F., Springer Netherlands, Dordrecht, 101–109, https://doi.org/10.1007/978-94-015-8190-5_12, 1993.

Nimbus Web Eventi Meteorologici: http://www.nimbus.it/eventi/2016/161125AlluvioniNordOvest.htm, last access: 10 June 2022.

660 Cevasco, A., Pepe, G., and Brandolini, P.: The influences of geological and land use settings on shallow landslides triggered by an intense rainfall event in a coastal terraced environment, Bulletin of Engineering Geology and the Environment, 73, 859–875, https://doi.org/10.1007/s10064-013-0544-x, 2014.

Cignetti, M., Godone, D., and Giordan, D.: Shallow landslide susceptibility, Rupinaro catchment, Liguria (northwestern Italy), 1–13, https://doi.org/10.1080/17445647.2019.1593252, 2019.

665   Conrad, O., Bechtel, B., Bock, M., Dietrich, H., Fischer, E., Gerlitz, L., Wehberg, J., Wichmann, V., and Böhner, J.:
           System for Automated Geoscientific Analyses (SAGA) v. 2.1.4, Geosci. Model Dev., 8, 1991–2007,
           https://doi.org/10.5194/gmd-8-1991-2015, 2015.

       Copernicus Climate Change Service: https://climate.copernicus.eu/ESOTC/2019/wet-end-year-western-and-southern-
           europe, last access: 29 April 2022.

670   Copernicus Open Access Hub: https://scihub.copernicus.eu/, last access: 8 June 2022.

       Cremonini, R. and Tiranti, D.: The weather radar observations applied to shallow landslides prediction: a case study
           from north-western Italy, 6, 134, https://doi.org/10.3389/feart.2018.00134, 2018.

       D'Amato Avanzi, G., Galanti, Y., Giannecchini, R., and Bartelletti, C.: Shallow Landslides Triggered by the 25 October
           2011 Extreme Rainfall in Eastern Liguria (Italy), in: Engineering Geology for Society and Territory - Volume
675   2, edited by: Lollino, G., Giordan, D., Crosta, G. B., Corominas, J., Azzam, R., Wasowski, J., and Sciarra, N.,
           Springer International Publishing, Cham, 515–519, 2015.

       Ferrari, F., Cassola, F., Tuju, P. E., and Mazzino, A.: RANS and LES face to face for forecasting extreme precipitation
           events in the Liguria region (northwestern Italy), Atmospheric Research, 259, 105654,
           https://doi.org/10.1016/j.atmosres.2021.105654, 2021.

680   Fiorucci, F., Cardinali, M., Carlà, R., Rossi, M., Mondini, A. C., Santurri, L., Ardizzone, F., and Guzzetti, F.: Seasonal
           landslide mapping and estimation of landslide mobilization rates using aerial and satellite images,
           Geomorphology, 129, 59–70, https://doi.org/10.1016/j.geomorph.2011.01.013, 2011.

       Fiorucci, F., Giordan, D., Santangelo, M., Dutto, F., Rossi, M., and Guzzetti, F.: Criteria for the optimal selection of
           remote sensing optical images to map event landslides, Nat. Hazards Earth Syst. Sci., 18, 405–417,
685   https://doi.org/10.5194/nhess-18-405-2018, 2018.

       Fiorucci, F., Ardizzone, F., Mondini, A. C., Viero, A., and Guzzetti, F.: Visual interpretation of stereoscopic NDVI
           satellite images to map rainfall-induced landslides, Landslides, 16, 165–174, https://doi.org/10.1007/s10346-
           018-1069-y, 2019.

       Gallus Jr, W. A., Parodi, A., and Maugeri, M.: Possible impacts of a changing climate on intense Ligurian Sea rainfall
690   events, International Journal of Climatology, 38, e323–e329, https://doi.org/10.1002/joc.5372, 2018.

       Gariano, S. L. and Guzzetti, F.: Landslides in a changing climate, Earth-Science Reviews, 162, 227–252,
           https://doi.org/10.1016/j.earscirev.2016.08.011, 2016.

       Ghorbanzadeh, O., Crivellari, A., Ghamisi, P., Shahabi, H., and Blaschke, T.: A comprehensive transferability
           evaluation of U-Net and ResU-Net for landslide detection from Sentinel-2 data (case study areas from Taiwan,
695   China, and Japan), Scientific Reports, 11, 14629, https://doi.org/10.1038/s41598-021-94190-9, 2021.

Giordan, D., Cignetti, M., Baldo, M., and Godone, D.: Relationship between man-made environment and slope stability: the case of 2014 rainfall events in the terraced landscape of the Liguria region (northwestern Italy), null, 8, 1833–1852, https://doi.org/10.1080/19475705.2017.1391129, 2017.

Gorelick, N., Hancher, M., Dixon, M., Ilyushchenko, S., Thau, D., and Moore, R.: Google Earth Engine: Planetary-scale geospatial analysis for everyone, Remote Sensing of Environment, 202, 18–27, https://doi.org/10.1016/j.rse.2017.06.031, 2017.

Govi, M.: Gli eventi alluvionali del 1977 in Piemonte: problemi di protezione idrogeologica, in: Proc. Conf."Pianificazione territoriale e geologia", Regione Piemonte–Dip. Organizzazione e gestione territorio e Assessorato Pianificazione Territorio, 37–45, 1978.

Guzzetti, F., Malamud, B. D., Turcotte, D. L., and Reichenbach, P.: Power-law correlations of landslide areas in central Italy, Earth and Planetary Science Letters, 195, 169–183, https://doi.org/10.1016/S0012-821X(01)00589-1, 2002.

Guzzetti, F., Cardinali, M., Reichenbach, P., Cipolla, F., Sebastiani, C., Galli, M., and Salvati, P.: Landslides triggered by the 23 November 2000 rainfall event in the Imperia Province, Western Liguria, Italy, Engineering Geology, 73, 229–245, https://doi.org/10.1016/j.enggeo.2004.01.006, 2004.

Handwerger, A. L., Huang, M.-H., Jones, S. Y., Amatya, P., Kerner, H. R., and Kirschbaum, D. B.: Generating landslide density heatmaps for rapid detection using open-access satellite radar data in Google Earth Engine, Nat. Hazards Earth Syst. Sci., 22, 753–773, https://doi.org/10.5194/nhess-22-753-2022, 2022.

IPCC, – Intergovernmental Panel on Climate Change: Climate Change 2014: Synthesis Report. Contribution of Working Groups I, II and III to the Fifth Assessment Report of the Intergovernmental Panel on Climate Change, Geneve, 2014.

Lanteaume, M., Radulescu, N., Gravos, M., Feraud, J., Faure-Muret, A., and Haccard, D.: Notice explicative, Carte Géologique de France (1/50.000), feuille Viève-Tende (948), 1990.

Lindsay, E., Frauenfelder, R., Rüther, D., Nava, L., Rubensdotter, L., Strout, J., and Nordal, S.: Multi-Temporal Satellite Image Composites in Google Earth Engine for Improved Landslide Visibility: A Case Study of a Glacial Landscape, 14, https://doi.org/10.3390/rs14102301, 2022.

Lu, P., Qin, Y., Li, Z., Mondini, A. C., and Casagli, N.: Landslide mapping from multi-sensor data through improved change detection-based Markov random field, Remote Sensing of Environment, 231, 111235, https://doi.org/10.1016/j.rse.2019.111235, 2019.

725 Luino, F.: The flood and landslide event of November 4–6 1994 in Piedmont Region (Northwestern Italy): Causes and
related effects in Tanaro Valley, Physics and Chemistry of the Earth, Part A: Solid Earth and Geodesy, 24,
123–129, https://doi.org/10.1016/S1464-1895(99)00007-1, 1999.

Mandarino, A., Luino, F., and Faccini, F.: Flood-induced ground effects and flood-water dynamics for hydro-
geomorphic hazard assessment: the 21–22 October 2019 extreme flood along the lower Orba River
730 (Alessandria, NW Italy), null, 17, 136–151, https://doi.org/10.1080/17445647.2020.1866702, 2021.

Martha, T. R., Kerle, N., Jetten, V., van Westen, C. J., and Kumar, K. V.: Characterising spectral, spatial and
morphometric properties of landslides for semi-automatic detection using object-oriented methods,
Geomorphology, 116, 24–36, https://doi.org/10.1016/j.geomorph.2009.10.004, 2010.

Meteologix: https://meteologix.com/it/precipitation/alessandria/calibrated-precipitation-total-6h/20191021-2050z.html,
735 last access: 27 May 2022.

Mondini, A. C., Guzzetti, F., Reichenbach, P., Rossi, M., Cardinali, M., and Ardizzone, F.: Semi-automatic recognition
and mapping of rainfall induced shallow landslides using optical satellite images, Remote Sensing of
Environment, 115, 1743–1757, https://doi.org/10.1016/j.rse.2011.03.006, 2011.

Notti, D., Wrzesniak, A., Dematteis, N., Lollino, P., Fazio, N. L., Zucca, F., and Giordan, D.: A multidisciplinary
740 investigation of deep-seated landslide reactivation triggered by an extreme rainfall event: a case study of the
Monesi di Mendatica landslide, Ligurian Alps, 1–25, https://doi.org/10.1007/s10346-021-01651-3, 2021.

Notti, D., Cignetti, M., Godone, D., and Giordan, D.: Semi-automatic and manual shallow landslide inventories of two
extreme rainfall events., https://doi.org/10.5281/zenodo.6617194, 2022.

Nowak, B., Marliac, G., and Michaud, A.: Estimation of winter soil cover by vegetation before spring-sown crops for
745 mainland France using multispectral satellite imagery, 16, 064024, 2021.

Paliaga, G. and Parodi, A.: Geo-Hydrological Events and Temporal Trends in CAPE and TCWV over the Main Cities
Facing the Mediterranean Sea in the Period 1979–2018, 13, https://doi.org/10.3390/atmos13010089, 2022.

Pepe, G., Piazza, M., and Cevasco, A.: Geomechanical characterization of a highly heterogeneous flysch rock mass by
means of the GSI method, Bulletin of Engineering Geology and the Environment, 74, 465–477,
750 https://doi.org/10.1007/s10064-014-0642-4, 2015.

Pepe, G., Mandarino, A., Raso, E., Cevasco, A., Firpo, M., and Casagli, N.: Extreme Flood and Landslides Triggered in
the Arroscia Valley (Liguria Region, Northwestern Italy) During the November 2016 Rainfall Event, in:
IAEG/AEG Annual Meeting Proceedings, San Francisco, California, 2018-Volume 1, 171–175, 2019.

Natural Hazards
and Earth System
Sciences
Discussions

Piana, F., Fioraso, G., Irace, A., Mosca, P., d'Atri, A., Barale, L., Falletti, P., Monegato, G., Morelli, M., Tallone, S.,
755   and Vigna, G. B.: Geology of Piemonte region (NW Italy, Alps–Apennines interference zone), null, 13, 395–
         405, https://doi.org/10.1080/17445647.2017.1316218, 2017.

QGIS Association.: QGIS.org, 2022. QGIS Geographic Information System. QGIS Association., 2022.

Qin, Y., Lu, P., and Li, Z.: LANDSLIDE INVENTORY MAPPING FROM BITEMPORAL 10 m SENTINEL-2
         IMAGES USING CHANGE DETECTION BASED MARKOV RANDOM FIELD, Int. Arch. Photogramm.
760   Remote Sens. Spatial Inf. Sci., XLII–3, 1447–1452, https://doi.org/10.5194/isprs-archives-XLII-3-1447-2018,
         2018.

R Core Team: R: A language and environment for statistical computing., R Foundation for   Statistical Computing,
         Vienna, Austria., 2020.

GEE Timeseries Explorer: https://geetimeseriesexplorer.readthedocs.io/en/latest/.

765 Land Cover Piemonte: https://www.geoportale.piemonte.it/geonetwork/srv/api/records/r_piemon:006cb751-4274-4ac3-
         a5bd-5bb3f1bbd251, last access: 8 June 2022.

Regione Piemonte - flood events 2019:
         http://www.sistemapiemonte.it/eXoRisorse/dwd/servizi/EventiAlluvionali/novembre2019/OCn3-A18-615-
         622-del-06042020.pdf, last access: 13 August 2021.

770 Roccati, A., Faccini, F., Luino, F., Turconi, L., and Guzzetti, F.: Rainfall events with shallow landslides in the Entella
         catchment, Liguria, northern Italy, Nat. Hazards Earth Syst. Sci., 18, 2367–2386,
         https://doi.org/10.5194/nhess-18-2367-2018, 2018.

Roccati, A., Paliaga, G., Luino, F., Faccini, F., and Turconi, L.: Rainfall Threshold for Shallow Landslides Initiation
         and Analysis of Long-Term Rainfall Trends in a Mediterranean Area, 11,
775   https://doi.org/10.3390/atmos11121367, 2020.

Rossi, M., Guzzetti, F., Reichenbach, P., Mondini, A. C., and Peruccacci, S.: Optimal landslide susceptibility zonation
         based on multiple forecasts, Geomorphology, 114, 129–142, https://doi.org/10.1016/j.geomorph.2009.06.020,
         2010.

Sassa, K., Fukuoka, H., Scarascia-Mugnozza, G., and Evans, S.: Earthquake-induced-landslides: distribution, motion
780   and mechanisms, 36, 53–64, https://doi.org/10.1016/j.sandf.2014.06.001, 1996.

Scheip, C. M. and Wegmann, K. W.: HazMapper: a global open-source natural hazard mapping application in Google
         Earth Engine, Nat. Hazards Earth Syst. Sci., 21, 1495–1511, https://doi.org/10.5194/nhess-21-1495-2021,
         2021.

Yu, B., Chen, F., and Muhammad, S.: Analysis of satellite-derived landslide at Central Nepal from 2011 to 2016,

785   Environmental Earth Sciences, 77, 331, https://doi.org/10.1007/s12665-018-7516-1, 2018.